Functional Dendritic Features of Serotonin Neurons in the Dorsal Raphe Nucleus

Jean-François Boucher

Thesis submitted to the University of Ottawa
in partial Fulfillment of the requirements for the
Master's degree in Neuroscience

Supervisor: Dr. Jean-Claude Béïque

Department of Cellular & Molecular Medicine
Faculty of Medicine
University of Ottawa

Abstract

The relatively few serotonin (5-HT) neurons located in the Dorsal Raphe Nucleus (DRN) give rise to an extensive axonal network modulating a wide-range of brain functions and behaviors. In turn, the DRN receives inputs from several brain regions and therefore exhibits the characteristics of a hub network. While recent technological advancements have provided an unprecedented look at the neurobiology of the DRN, important knowledge gaps remain in understanding how the constellation of synaptic inputs to this region confers 5-HT neurons their unique coding features. As a first step towards characterizing the DRN's input processing strategy, we set out to explore the landscape of dendritic operation operating in DRN 5-HT neurons. Using multi-photon microscopy and *in vitro* electrophysical recordings, we conducted a morphological and electrophysiological survey of 5-HT neurons where we identified two structurally and morphologically distinct types of glutamatergic synapses both expressing small NMDAR-mediated conductance. Our initial findings provide valuable insights on local rules that govern how synaptic inputs to the DRN are being processed to ultimately confer 5-HT neurons their unique coding features.

Acknowledgements

First and foremost, I would like to thank my supervisor, Dr. Jean-Claude Béïque, for his guidance, mentorship, and encouragement. I would also like to thank Dr. Joseph Erlichman and Dr. Ana Y. Estevez for introducing me to the world of neuroscience, and without whom I would not be the scholar I am today. This project would not have been possible without the work of a great number of my peers. The pioneering work done by Dr. Béïque, Michael Lynn, Emerson Harkin, Dr. Philippe Vincent-Lamarre, Dr. Érik Harvey-Girard, and Dr. Richard Naud, laid the foundation for the work presented here.

I would also like to extend a sincere thank you to Dr. Kirk Mulatz for technical assistance and input on the project. My thesis advisory committee members, Dr. Richard Naud and Dr. Tuan Bui, were instrumental in bringing this project into the light. Over the years, I valued their feedback which helped me continually improve my work.

I would also like to thank my evaluators, Dr. Richard Naud and Dr. Katalin Toth, for taking the time to read and assess my thesis.

An enormous thank you goes out to Michael Lynn, Emerson Harkin, Sébastien Maillé, Dr. Philippe Vincent-Lamarre, Léa Caya-Bissonnette, Dr. Anup Pillai, Éloise Valerie Giraud, and all the members of the Béïque, Naud, and Maler groups for helpful discussions and for having made my time at the lab incredible.

Finally, I would like to thank my family and, especially, my fiancé, Erica Catherine Newman, for all their support and patience throughout this long and arduous process that was writing a thesis while working full-time, and during a global pandemic.

Contents

List of figures

List of abbreviations

5CT 5-carboxamidotryptamine

5HT serotonin

AC adenylate cyclase

ACSF artificial cerebrospinal fluid

AMPA α-amino-3-hydroxy-5-methyl-4-isoxazolepropionic acid

bAP backpropagating action potential

CNS central nervous system

DIC differential-interference contrast

DRN dorsal raphe nucleus

EPSC excitatory post-synaptic current

EPSP excitatory post-synaptic potential

GABA γ-Aminobutyric acid

GFP green fluorescent protein

GPCR G-protein coupled receptor

MNI-GLU 4-methoxy-7-nitroindolinyl-glutamate

mPFC medial prefrontal cortex

MRN median raphe nucleus

NA numerical aperture

NMDA N-methyl-D-aspartate

PSD post-synaptic density

ROI region-of-interest

SERT serotonin transporter

sI/O subthreshold input-output

SOM somatostatin

TEA tetraethylammonium

TTX tetrodotoxin

1. Introduction

1.1 Dorsal Raphe organization and function

The ability to synthesize and release serotonin (5-hydroxytryptamine; 5-HT) is only shared by less than 0.1% neurons in the human's central nervous system (Baker et al., 1990, 1991; Okaty et al., 2019). Despite their small numbers, 5-HT-containing neurons are involved in the modulation of a wide array of central nervous system functions including, but not limited to, locomotion (Correia et al., 2017), anxiety-like behaviors (Marcinkiewcz et al., 2016; Ren et al., 2018), active-coping behaviors (Ren et al., 2018; Warden et al., 2012), patience for future rewards (Fonseca et al., 2015; Li et al., 2016; Lottem et al., 2018; Miyazaki et al., 2018, 2014), reward prediction (Iigaya et al., 2018; Matias et al., 2017; Zhou et al., 2017), and processing of reward and punishment signals on multiple timescales (Cohen et al., 2015). 5-HT neurons populate the raphe nuclei, divided into 9 brainstem nuclei labeled B1 to B9 on a rostrocaudal axis (Dahlström and Fuxe, 1964). Of those nuclei, the dorsal raphe nucleus (DRN; groups B6 and B7) and the median raphe nucleus (MRN; groups B5 and B8) account for mostly all the ascending serotonergic projections to the midbrain and forebrain (Fernandez et al., 2016; Huang et al., 2019; Okaty et al., 2020; Ren et al., 2018, 2019). The DRN contains approximately 8,000 to 10,000 5-HT neurons, in the mouse brain, and 12,000 to 15,000 5-HT neurons, in the rat brain, accounting for more than half of the whole serotonergic population (Ishimura et al., 1988; Jacobs and Azmitia, 1992). Acknowledged as a potent regulator of emotion and mood, the serotonergic system is the target of many treatments for behavioral and psychological disorders, but detailed mechanistic understanding about its functions in the brain still lacks.

The nature of the overall information stream that is encoded by 5-HT neurons and broadcasted to the brain during behavior is still unclear. The population activity of DRN 5-HT

neurons in response to emotionally salient stimuli have been monitored using a number of experimental approaches surveyed in an effort to understand its role in the modulation of emotional valence states. The heterogeneous, and sometimes conflicting, population responses to aversive as well as rewarding stimuli (Cohen et al., 2015; Li et al., 2016; Luo et al., 2016; Zhong et al., 2017) has still not resulted in the development of a unifying theoretical framework on the role of DRN 5-HT neurons. Consequently, the idea of the DRN 5-HT population acting as a monolithic whole faded away giving rise to a wave of research focused on 5-HT neuron diversity and function. Recently, studies using viral vector strategies capable of targeting subgroups as well as individual DRN 5-HT neurons, in animal models, has produced a comprehensive map of the DRN's inputs and outputs (Fernandez et al., 2016; Ogawa et al., 2014; Pollak Dorocic et al., 2014; Ren et al., 2018, 2019; Weissbourd et al., 2014; Zhou et al., 2017). This map revealed the complexity and diversity of the projection pattens of 5-HT neurons. 5-HT axon terminals have been showed to innervate numerous cortical brain regions (including olfactory bulb, piriform cortex, cortical amygdala, prefrontal cortex, motor cortex, somatosensory cortex, retrosplenial cortex, auditory cortex, visual cortex, entorhinal cortex, perirhinal cortex, and ectorhinal cortex), the basal ganglia, the amygdala, the hypothalamus, the thalamus, the brainstem, and the cerebellum (Fernandez et al., 2016; Ogawa et al., 2014; Pollak Dorocic et al., 2014; Ren et al., 2018, 2019; Weissbourd et al., 2014; Zhou et al., 2017). Additionally, recent taxonomic studies, using high-throughput single-cell transcriptomics and intersectional genetic tools, assembled a detailed atlas of the anatomical and molecular diversity of the dorsal raphe serotonergic system (Huang et al., 2019; Okaty et al., 2020; Ren et al., 2019). Taken together, these studies have established a cartography of the DRN that illustrates the presence of several 5-HT neuron subnetworks, or modules, based on afferent and efferent connections, molecular and cellular properties, and spatial organization, in turn

providing researchers with an unprecedented look at the neurobiology of the dorsal raphe. Upon its release on postsynaptic target regions, 5-HT interacts with an impressive diversity of G-protein-coupled receptors (GPCRs) and ligand-gated receptors (Okaty et al., 2019). Currently, there are seven families of 5-HT receptors, based on pharmacology, transduction and structure, and those families each possess multiple subtypes. The 5-HT GPCR receptors are subdivided into groups (or families) based on their coupling to second messengers via the G-proteins (Filip and Bader, 2009; Hannon and Hoyer, 2008). For instance, the 5-HT_1 receptor family (including 5-HT_{1A}, 5-HT_{1B}, 5-HT_{1D}, and 5HT_{1F}) are mostly linked to $G_{i/o}$-protein which couple negatively to adenylate cyclase (AC), in turn may lead to decrease cell activity (Filip and Bader, 2009; Hannon and Hoyer, 2008). Most notably, the 5-HT_{1A} receptors have been showed to mediate neuronal hyperpolarisation via G-protein coupled K^+ channels (GIRK channels) and ultimately inhibit neuronal firing (Filip and Bader, 2009; Hannon and Hoyer, 2008). In the DRN, the 5-HT receptors are also express on 5-HT cells, and when activated, inhibit 5-HT cell firing and 5-HT release (Filip and Bader, 2009; Hannon and Hoyer, 2008). The other families of GPCRs include the 5-HT_2 receptors (including 5-HT_{2A}, 5-HT_{2B} and 5-HT_{2C}) coupled with $G_{q/11}$-protein, the 5-HT_4 receptors (including 5-HT_{4a}–5-HT_{4n}), 5-HT_5 receptors (including 5-HT_{5A} and 5-HT_{5B}), and 5-HT_6 all coupled with G_s-protein (Filip and Bader, 2009; Hannon and Hoyer, 2008). Interestingly, the 5-HT_7 receptors are also GPCRs, however it does not fit with the known 5-HT_1 or 5-HT_2 receptor types, neither does it fit with any of other GPCRs families; for a number of years it was known as 5-HT_1–like and remained rather elusive (Filip and Bader, 2009; Hannon and Hoyer, 2008). Last, but not least, the only fast-acting ligand-gated ion channel receptor, the 5-HT_3 receptors are non-selective cation channels and trigger rapid depolarization when activated (Filip and Bader, 2009; Hannon and Hoyer, 2008). These ionotropic receptors have also been showed to rapidly desensitize and re-sensitize (Filip and

Bader, 2009; Hannon and Hoyer, 2008). The extensive work focused on the 5-HT system has revealed layers of functional complexity and compositional heterogeneity warranting a more nuanced view of the DRN. Elucidating how the molecular, neurochemical, anatomical, hodological, electrophysiological characteristics of 5-HT neurons overlap to give rise to the DRN's function becomes essential in understanding its role in the brain.

1.2 Understanding the synaptic rules governing DRN input processing

The DRN is an extensively connected hub-network in the mammalian brain, well positioned to process a variety of incoming, and at times, competing inputs and to widely regulate mood and behavior. Continuously receiving a wealth of information about internal and external variables from multiple brain regions, DRN 5-HT neurons must rapidly process this large, and diverse, synaptic workload to tune serotonin output. As such, the firing of a relatively small number of 5-HT neurons is poised to regulate the excitability of large ensembles of neural networks implicated in several brain functions. In this section, we will discuss input processing mechanisms employed by DRN 5-HT neurons.

The transformation of various, and sometimes competing, inputs into a cohesive output represents a formidable computational task for the DRN. Because there are so many inputs, an essential feature of this transformation is to discard the irrelevant information and select only the relevant information. Similar to an algorithm in computer science, where a sequence of simple computational operations organized in a flowchart leads from the input to the output, neuronal firing is informed by neuronal computations, in turn, shaped by many different sequences of neuronal operations (London and Häusser, 2005). The range of dendritic operations available to a neuron is directly influenced by the properties of its primary input site, the dendritic tree. An electrical signal propagating through a passively conducting dendrite versus an actively conducting

dendrite will undergo different types of neuronal operations. For instance, in a passive dendrite, the voltage's amplitude and time course will slowly decrease over time and distance resulting in an operation known as dendritic filtering (London and Häusser, 2005; Rall, 1967; Tran-Van-Minh et al., 2015). In this scenario, a synaptic input originating near the soma will enact a more powerful regulation of a neuron's excitability, and it is more likely to influence the neuron's action potential firing behavior than an input of similar weight located more distally. Such a neuron can, using this simple dendritic operation, discriminate between synaptic inputs located at various distance along a dendritic segment. However, input currents are likely exposed to a wide array of different dendritic operations, leading to many possible dendritic operation sequences (or algorithms), and a corollary augmentation of the computational power of neurons. The exceptional input processing power of individual neurons is on constant display throughout the brain. For instance, and illustrating this point, recent studies of the retinal direction-selective ganglion cells demonstrated that the spatiotemporal pattern of inhibition and excitation onto their dendritic tree strongly shaped direction selectivity, independently, within individual dendritic branches (Jain et al., 2020). The mounting knowledge on dendritic operations and neuronal computations has led to the formulation of synaptic rules helping to predict how certain spatiotemporal patterns of synaptic activity influence the firing of neurons. Critically, these dendritic operations are cell type specific. Although recent years have provided an abundance of information on the molecular, anatomical, and electrophysiological properties of 5-HT neurons (Okaty et al., 2020), the current knowledge of the dendritic properties of 5-HT neurons and the dendritic operations they utilized to process the DRN's various, and sometimes competing, inputs remain scarce. The Béïque laboratory's interest has focused on this gap in knowledge with the objective to identify the synaptic rules that

best describe how DRN afferent inputs regulate the release of a ubiquitous neurotransmitter with persuasive influence across several brain regions.

Past and ongoing work in the Béïque laboratory has provided key insights into the neural computations performed by the DRN and 5-HT neurons. *Geddes et al.* (2016) examined projections from the medial prefrontal cortex (mPFC) to both DRN 5-HT neurons and local GABAergic interneurons. These results showed that serotonin neurons received both classical monosynaptic excitations, as well as strong feed-forward inhibition enacted through local GABAergic interneurons. Yet, they also uncovered a target-specific neuromodulatory mechanism responsible for the shifting of excitatory balance in favor of the mPFC inputs to serotonin neurons. Elevated endocannabinoids disproportionally reduced the monosynaptic excitation onto GABAergic interneurons leading to a dominant monosynaptic activation of 5-HT neurons. These results demonstrated how local microcircuits and transient neuromodulation within DRN can powerfully modulate long-range inputs but leave open the question of whether dendritic mechanisms within serotonin neurons provide a further layer of filtering to these inputs.

Harkin et al. (2021) characterized the computational properties of the DRN using an ingenious approach combining electrophysical recordings with network simulations to create experimentally-constrained models of the two most abundant cell types in the dorsal raphe (i.e. 5-HT and GABAergic somatostatin (SOM) neurons). The computational models provided key insights on neural computations of the DRN network emerging from excitability features of these constituent neurons. This study found that potent adaption mechanisms, and strong A-type potassium current (I_A), in individual 5-HT neurons, in addition to the feed-forward mechanism, were powerful regulators of the DRN population response to phasic and tonic synaptic inputs. Most notably, the work collected strong computational evidence demonstrating that the peak 5-

HT neuron population firing rate linearly reported the derivative of the synaptic inputs to the DRN, linking a set of cellular properties with an emergent network computation. This study is among the few tackling the long-standing discussion of the computational roles of the DRN by using a bottom-up approach; identifying specific cellular and network mechanisms that give rise to network-level computations performed by the DRN, ultimately supporting its role in guiding a wide-range of behaviors.

Despite the Béïque laboratory's ongoing efforts to characterize the DRN's input processing strategy, important knowledge gaps remain. Many elemental computational questions are still left unanswered. For instance, is a 5-HT DRN neuron capable of functionally discriminating between two, or more, excitatory inputs, or alternately are all excitatory synapses treated equivalently by single neurons despite each communicating distinct information over multiple timescales? In a hub network, such as the DRN, the ability of single cells to preserved *relevant* informational content from more than one input and relay it downstream to the network for decoding is highly beneficial. Previous studies in other systems like the fly visual system (Fairhall et al., 2001), the electrosensory system in fish (Benda et al., 2006; Chacron and Bastian, 2008), or in the mammalian cortex (Naud and Sprekeler, 2018) have successfully identified neural strategies where two distinct stimuli can be discriminated and represented in parallel in a spiking output. A study has already provided strong evidence that 5-HT neurons can perform multiplexing operations to process reward and punishment over multiple time scales (Cohen et al., 2015). However, we pondered what specific dendritic computational operations allow 5-HT neurons to access those neural strategies.

1.3 Dendritic computations in DRN 5-HT neurons

Early theoretical studies hypothesized that dendrites possessed properties capable of influencing the way neurons integrate synaptic inputs (Koch et al., 1983; Rall, 1964). With increasing technical sophistication, several experimental studies have demonstrated that, indeed, dendrites do perform a slew of computational operations in response to dynamic inputs, rapidly selecting the relevant information that will be sent to, read out, and stored by downstream networks (Larkum et al., 2009; Takahashi et al., 2016; *Reviewed in* Stuart and Spruston, 2015). Many of those studies used brain slices and culture preparations due to the direct access to the biophysical features of the dendritic tree. Yet, in an integrating hub such as the DRN, studying how complex spatiotemporal patterns of synaptic inputs drive neuronal spiking presents many technical challenges, one of which being how to control the timing and spatial location of incoming synaptic inputs to study how changing these variables affect neuronal spiking behaviors. The Béïque laboratory's expertise in two-photon microscopy, glutamate uncaging, and whole-cell electrophysiology (Béïque et al., 2006, 2007, 2011; Lee et al., 2016; Soares et al., 2013, 2017), provided the necessary tools to overcome this obstacle, and so, ideally positioned us to study the synaptic and dendritic mechanisms used by DRN 5-HT neurons to discriminate between distinct inputs.

Multi-photon glutamate uncaging uses a fast-pulsing laser (i.e. femtosecond pulsed laser) to photolyze (i.e. uncage) a caged glutamate compound (i.e. MNI-Glutamate) close to a putative glutamatergic synapse, mimicking chemical neurotransmission. Synthesized by both Dr. Ellis-Davies and the Corrie laboratory, in 2000, MNI-Glutamate makes use of a photochemical "caging compound" (e.g. 4-methoxy-7-nitroindolinyl; MNI) covalently attached to a neurotransmitter rendering it inert (Matsuzaki et al., 2001; Papageorgiou and Corrie, 2000; *Reviewed in* Ellis-Davies, 2019). Laser irradiation breaks the covalent bond, releasing the caged biological molecule in the extracellular milieu. In the case of MNI-Glutamate, the resulting uncaging event evokes an

excitatory post-synaptic response when the uncaged glutamate binds to glutamatergic ionotropic receptors, in close proximity. The local synaptic event can, in turn, be visualized by recording the postsynaptic cell in whole-cell patch clamp configuration. By capitalizing the relative ease of controlling light in both space and time, this approach allows the experimenter to emulate synaptic transmission at will, while having control over the spatiotemporal parameters of the synaptic inputs.

By mimicking the synaptic activation occurring within the dendritic tree using a focused laser beam to locally liberate neurotransmitter, and systematically probing the neuron's voltage response, we were able to create an experimental environment where synaptic activation was near what is thought to occur *in vivo*. Although recent electrophysiological (Cohen et al., 2015) and optical (Li et al., 2016; Matias et al., 2017; Ren et al., 2018; Zhong et al., 2017) techniques allow for the recording of electrical and chemical dendritic signaling in awake and freely moving animals, a slice preparation remains a valuable tool because of its higher subcellular resolution, and the prevention of confounding variables that are present with *in vivo* experiments (e.g. movement artifacts,). Together, these characteristics make *in vitro* whole-cell electrophysical recordings, multi-photon microscopy and glutamate uncaging, unparallel tools for our eventual goal of defining the synaptic rules that govern how inputs are being process by 5-HT neurons to regulate the DRN's widespread outputs.

1.4 Summary

The hub-network architecture of the DRN supports its important role in regulating various brain functions, but also warrants for a detailed survey of the building blocks making up its computational toolbox. Technological advancements granted researchers with unprecedented access to the DRN facilitating a shift towards an unified understanding of its behavioral role, yet,

many questions still remain. Namely, what are the dendritic operations responsible for the transformation of long-range inputs to DRN into a cohesive serotonin output? Driven by this, albeit daunting, question, we set out to explore the landscape of dendritic operation operating in DRN 5-HT neurons. Using multi-photon microscopy and *in vitro* electrophysical recordings, we found evidence of two structurally and morphologically distinct putative glutamatergic synapses on 5-HT dendrites. Next, we characterized the subcellular glutamatergic receptor compositions at each putative synaptic site, investigating potential biophysical differences between the synaptic sites. Finally, we surveyed how the distance of a synaptic input, in relation to the soma, contributed to the processing of spatially varying inputs.

2 Materials and Methods

2.1 Experimental procedures

2.1.1 Animals

Experiments were performed on male and female C57/Bl6 mice aged 4-8 weeks expressing the fluorescent marker TdTomato under the control of the SERT promoter. Animals were group housed and kept on a 12:12-h light/dark cycle with access to food and water ad libidum. All experiments were carried out in accordance with procedures approved by the University of Ottawa Animal Care and Veterinary Services.

2.1.2 Acute midbrain slice preparation

Animals were deeply anaesthetized using isofluorane (Baxter Corporation) before being euthanized by decapitation. The brain was quickly removed from the skull into ice-cold choline dissection buffer containing (in mM) 119.0 choline chloride, 2.5 KCl, 4.3 $MgSO_4$, 1.0 $CaCl_2$, 1.0

NaH_2PO_4, 1.3 Na ascorbate, 11.0 glucose, 26.2 $NaHCO_3$ saturated with 95% O_2/5% CO_2 (pH = 7.3; 295-300 mOsm/L). A Leica VT1000S vibratome was used to cut 300 µm sections of the DRN in the same ice-cold choline dissection buffer. After cutting, slices were placed in a recovery chamber filled with standard artificial cerebrospinal fluid (ACSF) containing (in mM) 119.0 NaCl, 2.5 KCl, 1.3 $MgSO_4$, 2.5 $CaCl_2$, 1.0 NaH_2PO_4, 11.0 glucose, 26.2 $NaHCO_3$ maintained at 37°C, and continuously bubbled with 95% O_2/5% CO_2 (pH = 7.3; 290-295 mOsm/L). The recovery chamber was allowed to equilibrate to room temperature for 1 h before beginning recording.

2.1.3 In vitro whole-cell electrophysiology

The same ACSF was used in all whole-cell electrophysiology experiments, with additional drugs added as described in the text (500 nM tetrodotoxin (TTX), 100 nM 5-carboxamidotryptamine (5-CT); Abcam). For the voltage clamp experiment to probe AMPA/NMDA ratios at synapses, electrodes were filled with an intracellular solution (pH = 7.2-7.3; 270-290 mOsm/L) containing (in mM) 115 cesium methane-sulfonate, 0.4 EGTA, 5 tetraethylammonium-chloride (TEA-Cl), 6.7 NaCl, 20 HEPES, 3 ATP-Mg, 0.5 GTP, 10 Na-phosphocreatine (all purchased from Life Technologies), 5 QX-314 (Abcam). For current-clamp uncaging experiments, electrodes were filled with a K-gluconate based solution containing (in mM): 115 K-gluconate, 20 KCl, 10 HEPES, 4 ATP-Mg, 0.5 GTP, 10 Na-phosphocreatine (pH = 7.2-7.3; 270-290 mOsm/L). Intracellular solutions were supplemented with 2.5 µM Alexa Fluor-594 (Life Technologies) to visualize morphology.

2.1.4 Two-photon imaging and glutamate uncaging

Midbrain slices were placed in a recording chamber and cells in the DRN were visualized under differential-interference contrast (DIC) on an Olympus MPE-1000 system (BX61WI upright

microscope Olympus Canada, Toronto, ON) 60x/1.0NA objective. Whole-cell recordings were performed with an Axon Multiclamp 700B amplifier, and signals were filtered at 2 kHz and digitized with an Axon Digidata 1440A at 10 kHz (Molecular Devices, USA). Borosilicate glass recording electrodes with resistances ranging from 3-5 MΩ were pulled using a Narashige PC-10 vertical puller (Narishige, Japan). Access resistance was monitored with a 5 mV hyperpolarizing step at the beginning of each recording sweep. Glutamate uncaging experiments were performed with 2.5 mM MNI-glutamate-trifluoroacetate (Femtonics, Hungary) added to the extracellular solution. Neurons were imaged >3 mins after break-in. Simultaneous two-photon imaging and glutamate uncaging was performed using two ultrafast Ti:Sapphire pulsed lasers with pre-chirp compensation (MaiTai DeepSee, Spectra Physics, USA) coupled to a galvanometer scanning system (Olympus MPE-1000) and two independent acousto-optic modulators. Image acquisition and stimulation patterns were controlled using Olympus FV-1000 software. One laser was tuned to 810 nm to visualize Alexa Fluor 594, and the second laser was tuned to 720 nm for glutamate uncaging.

Synaptic stimulation was carried out by 2P glutamate uncaging at identified dendritic spines or dendritic shaft "current hotspots". In voltage-clamp at a holding potential of -70 mV, the intensity of the uncaging laser was tuned to generate ~15 pA AMPAR-mediated EPSCs for each ROI. The laser power was maintained in subsequent experiments to probe synaptic responses. For current-clamp experiments, somatic current injection was used in most cases to maintain stable membrane potential at -70 mV, and cells were discarded if more than 100 pA of current was required. Z-stack reconstructions were collected for neuron morphology analysis.

For uncaging-evoked AMPA/NMDA ratio, the intensity of the uncaging laser was tuned to first generate 10-30 pA AMPA-mediated EPSC at a holding potential of -70 mV and the mixed

AMPA and NMDA-mediated EPSCs was subsequently measured at a holding potential of +40 mV using the same uncaging laser power. The AMPAR-mediated component was given by the peak amplitude of the outward current measured at V_m = +40 mV aligned to the peak amplitude of the inward current at V_m = -70 mV, and the NMDAR-mediated component was estimated by the amplitude of the outward current at V_m = +40 mV, at a time when the current at V_m = -70 mV had decayed (~3x tau). This technique minimized the distortion to the AMPA/NMDA ratio due to space-clamp problems.

2.2 Computational methods

2.2.1 Ball-and-Stick model

Simulations were performed using NEURON 7.2 software and Python 3.5 scripts. The ‘‘ball-and-stick’’ models consisted of a cylindrical soma (10 mm length by 10 mm diameter) and a dendrite (400 µm long with segments of 1 µm). Cytoplasmic resistivity (R_i), and specific membrane capacitance (C_m) in all models were set to 100 Vcm, and 1 mF/cm^2, respectively, and resting membrane potentials were set to -70 mV. Specific membrane resistance (R_m) was set to 75,000 Vcm^2 (Harkin et al., 2021). AMPA-like EPSPs were generated by conductance changes (max conductance = 500 pS) with a reversal potential of 0 mV and exponential rise (tau = 0.2 ms) and decay (tau = 2 ms).

2.2.2 Morphological Analysis

Images of the neurons were taken at 512 x 512 pixels and were reconstructed using ImageJ Z project function. The morphological features (e.g., Dendrite caliber) were extracted using the NeuroAnatomy plugin. Dendritic images were taken at 256 x 256 pixels and were reconstructed using ImageJ as well. Spines were manually counted, and spine density was given by dividing the

number of protrusions emanating from the dendrite in the *xy* plane by the total length of dendrite examined (at least 20 μm per dendrite). Brightness and contrast were enhanced for representative images only.

2.2.3 Data analysis and statistical analysis

Data analysis was carried out using Python 3.5 scripts that were custom written. The following third-party Python packages were used: numpy and numba for numerical simulations (van der Walt et al., 2011); scipy for signal processing (Jones et al., 2001); and matplotlib and seaborn for figure creation. Statistical analysis was carried out using R 4.0 scripts that were custom written. The statistical tests are indicated in the text, and statistical significance was assessed at $p < 0.05$.

3 Results

3.1 Physiology and morphology of DRN 5-HT neurons

As a first order of business, we carried out *in-vitro* electrophysiological recordings of Td-Tomato-labelled 5-HT neurons in the whole-cell patch clamp configuration to survey the electrophysiological properties of serotonergic cells located in the dorsal raphe. Alexa-594 fluorescent was including in the intracellular recording solution, approximately 3 minutes following break-in, the dye fully diffused through the dendritic tree. Including the fluorescent dye Alexa 594 further allowed to examine morphological features of these neurons. At first glance, their bipolar cell bodies and poorly branching dendritic arborizations (Figure 1B) were rather unremarkable, yet DRN 5-HT neurons have distinct electrophysiological properties and morphological features setting them apart from non-serotonergic neurons in the dorsal raphe (Li et al., 2001). Electrophysiologically, the spiking behavior of DRN 5-HT neurons was highlighted by several features, including a marked latency to the first spike (Figure 1C). Published data from

the Béïque laboratory demonstrated that the delay in firing onset arose, in part, from the expression of a potassium current, identified as I_A, which exhibited a large outward current in response to voltage steps from -80 mV to near spike threshold (Figure 1D) (Harkin et al., 2021). As previously reported, the application of 5-carboxamidotryptamine (5-CT) elicited a hyperpolarizing current (Figure 1E), indicating that these neurons express $5HT_{1A}$ receptors (Geddes et al., 2015). Morphologically, DRN 5-HT neurons had a bipolar or multipolar shape with small caliber tapering primary dendrites (Fig. 1G, < 50 µm : 2.03 ± 0.284 µm, > 50 µm : 1.26 ± 0.0588 µm, n = 7, p = 0.01563, Wilcoxon signed-rank test). Most notably, DRN 5-HT neurons possessed dendritic spines, with a density of approximately 1 spines per 10 µm, and the spine density remained comparable along the length of the dendrite (Fig. 1H, < 50 µm : 1.92 ± 0.263 spines/ 20 µm, > 50 µm : 2.44 ± 0.220 spines/ 20 µm, n = 7, p = 0.2188, Wilcoxon signed-rank test). Although nonsignificant in our data set, we observed an increased in the spine density of distal dendrites, a morphological feature previously reported with DRN 5-HT neurons (Li et al., 2001). From the initial survey of the morphological features of DRN 5-HT neurons, one dendritic property stood apart for its potential impact on neuronal computations: the sparse spine density. The prevalence of spines on the dendritic tree of spiny neurons as well as their contribution to enhancing connectivity, the non-saturation of excitatory inputs, and input-specific synaptic plasticity has made them one of the canonical features of dendrites (Yuste, 2011). Why a neuron receiving so many competing inputs, such as a DRN 5-HT neuron, does not maximize its spine density to exploit those input processing benefits? Compelled with the eagerness to find the utility of this hallmark of DRN 5-HT neurons, we turned our attention to how an individual 5-HT neuron integrate its synaptic inputs.

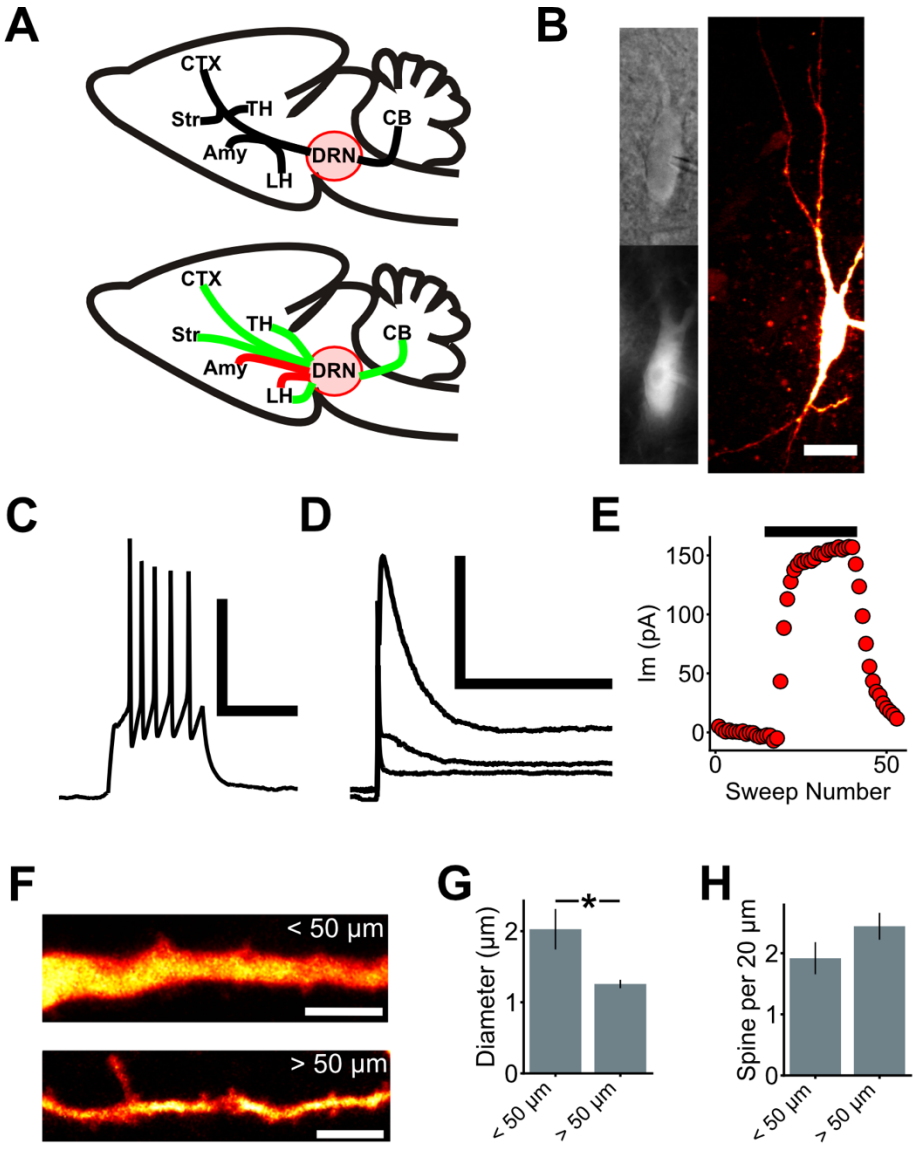

Figure 1. Physiology and morphology of serotonin neurons.
(A) Long-range connectivity patterns of DRN 5-HT neurons. Long-range projections (top) and long-range inputs (bottom). Red represents GABAergic inputs and green represents glutamatergic inputs. Amygdala (Amy), lateral hypothalamus (LH), prefrontal cortex (CTX), striatum (Str), thalamus (TH), cerebellum (CB). (B) Identification of 5-HT neurons. DIC (top left), fluorescence (bottom left) imaging showing Cre-dependent expression of TdTomato, and multi-photon image (right) of a DRN 5-HT neuron with morphological marker Alexa 594 (scale bar; 20 µm). (C) Spiking characteristics (scale bar; 50 mV/200 ms). (D) Whole-cell currents in TTX (scale bar; 600 pA/200 ms). (E) 5HT neurons express 5HT1A receptors. Bar represents the 5CT wash-in. (F) DRN 5-HT dendrite (scale bar; 5 µm). (G) Dendrite diameter in proximal (first 50 µm) and distal (remaining length) dendrites. (H) Spine density in proximal (first 50 µm) and distal (remaining length) dendrites.

3.2 Validation of multi-photon glutamate uncaging in DRN serotonin neurons

Whole-cell electrophysical recordings, in combination with multi-photon microscopy and glutamate uncaging, granted visualization of dendritic morphology with subcellular resolution (i.e. individual spine and shaft synapses), single-synapse activation with high spatiotemporal precision, and thus, allowed us to study how dendritic features impact synaptic integration (Figure 2A). First, the genetically identified 5-HT neurons were recorded and fluorescently labeled with Alexa-595. Following the complete diffusion of the fluorescent dye, using a laser tuned to a wavelength of 810 nm, a region-of-interest (ROI) was selected close to a putative glutamatergic synapse (Figure 2B) for initial screening. With 2.5 mM MNI-caged glutamate in the extracellular solution, 1 ms laser pulses, using a second laser tuned to 720 nm, were directed near the ROI. If the photolyzed MNI-Glutamate successfully triggered a local excitatory event, which in turn, travelled to soma generating an excitatory post-synaptic potential (EPSP) recorded by our whole-cell patch clamp, the ROI was eligible for further experimentations.

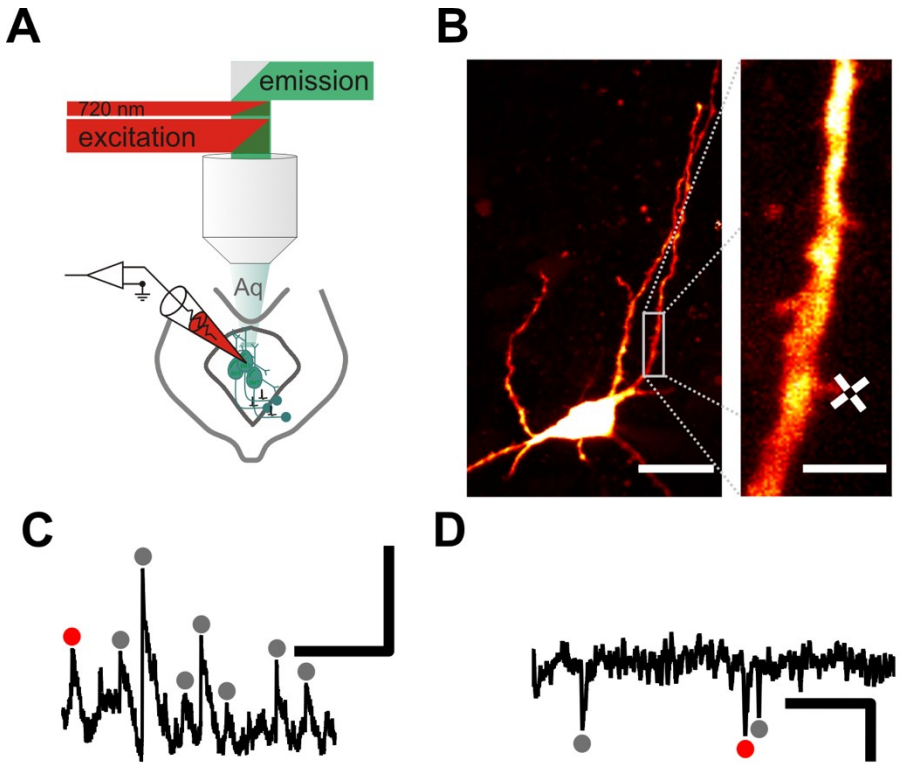

Figure 2. Multi-photon glutamate uncaging on DRN 5-HT neurons.
(A) Schematic illustration of whole-cell electrophysiological recording, in combination with multi-photon microscopy, of DRN 5-HT neurons. (B) Multi-photon image of a DRN 5-HT neuron with morphological marker Alexa 594 (scale bar; 25 µm). High-magnification image of the dendritic segment (right) marked by the white box. The uncaging ROI is shown by the white crosshair. (scale bar; 5 µm) (C) Current-clamp recording trace (scale bar; 1 mV/1 sec). The red dot shows an uncaging-evoked excitatory post-synaptic potential (uEPSP). The grey dots show spontaneous excitatory post-synaptic potentials (sEPSPs). (D) Voltage-clamp recording trace (scale bar; 10 pA/200 ms). The red dot shows an uncaging-evoked excitatory post-synaptic current (uEPSC). The grey dots show spontaneous excitatory post-synaptic currents (sEPSCs).

By recording the membrane potential in current clamp, over several seconds, we were able to concomitantly record spontaneous excitatory post-synaptic responses and uncaging-evoked excitatory post-synaptic responses (Figure 2C-D) allowing for the comparison between spontaneously occurring and experimentally elicited synaptic events. To ensure the uncaging-evoked excitatory post-synaptic potentials (uEPSPs) respected the physiological-bounds of synaptic neurotransmission, we evaluated if their characteristics resembled the ones of spontaneous excitatory post-synaptic responses (sEPSPs). The mean amplitude (Fig. 3A, uEPSPs:

1.40 ± 0.166 mV, n = 27; sEPSPs: 1.40 ± 0.01 mV, n = 22; p = 0.9868, Student T-test), and mean rise time (Fig. 3B, uEPSPs: 4.36 ± 0.374 ms, n = 27; sEPSPs: 5.17 ± 1.18 ms, n = 22; p = 0.5208, Student T-test) were comparable between uEPSPs and sEPSPs. The decay tau, however, was not comparable between uEPSPs and sEPSPs (Fig. 3C, uEPSPs: 46.9 ± 3.25 ms, n = 27; sEPSPs: 82.8 ± 5.74 ms, n = 22; $p < 0.05$, Student T-test). The uEPSPs demonstrated a significantly faster decay phase. A prominent determinant of the time course of post-synaptic events is the deactivation of glutamatergic receptors (i.e., NMDARs and AMPARs) (Edmonds et al., 1995; Jonas and Spruston, 1994). The deactivation kinetics of NMDARs and AMPARs are affected by multiple factors, such as neurotransmitter concentration in the synaptic cleft and subunit receptor composition (Edmonds et al., 1995; Jonas and Spruston, 1994). Although we controlled for the concentration of MNI-Glutamate responsible for triggering uEPSPs, it was impossible to control for the concentration of endogenous glutamate responsible for triggering sEPSPs. To investigate if the neurotransmitter concentration in the synaptic cleft during sEPSPs and uEPSPs differed, we compared the mean amplitude of spontaneous post-synaptic currents (sEPSCs) to the mean amplitude uncaging post-synaptic currents (uEPSCs) in voltage clamp (-70 mV). In this scenario, the amplitude of EPSCs is proportional to the number of AMPARs recruited by the nearby glutamate, and thus, gives an approximate measure of the concentration of glutamate in the synaptic clef. The average amplitude of sEPSCs did not differ from the uEPSCs amplitude (Fig. 3D, uEPSCs: 15.6 ± 0.885 pA, n = 27; sEPSCs: 16.0 ± 1.34 pA, n = 26; p = 0.8045, Student T-test), and was similar to the previously reported spontaneous EPSC amplitude onto DRN 5-HT neurons (Geddes et al., 2015). We recognized our approach to measuring the concentration of glutamate to be rudimentary, nevertheless, we felt it was enough to demonstrate a comparable amount of glutamate was present during sEPSPs and uEPSPs and did not cause the difference in time course we observed. In

principle, differences in subunit composition of AMPARs and NMDARs is a potential interpretation that assumes that the sEPSCs and uEPSC are not being sampled from the same population (eg., proximal vs distal). sEPSCs occurring at varying distances from the soma, or on different morphological and structural dendritic locations can affect the time course of the sEPSPs observed at the soma. Contributing factors that we will be examining experimentally later in our study. Altogether, the synaptic-like uncaging responses reliably captured the characteristics of physiological responses validating our principal experimental approach to study single-synapse input processing in DRN 5-HT neurons.

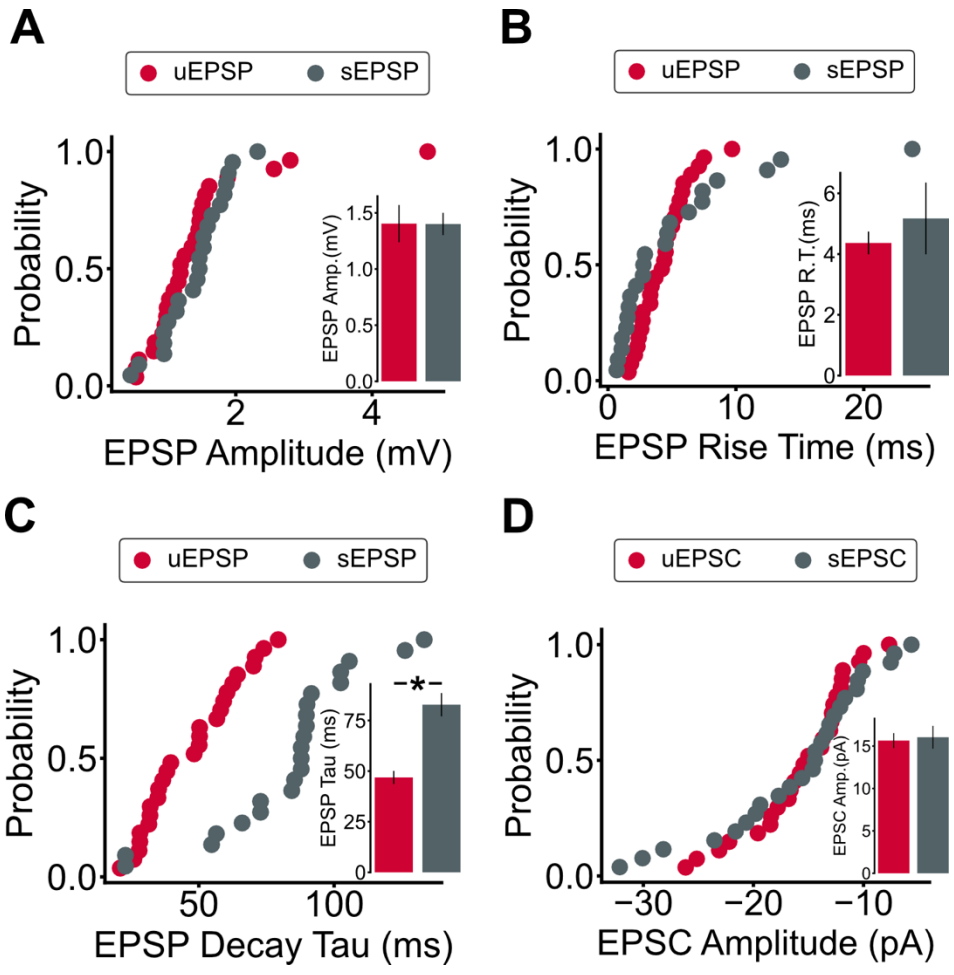

Figure 3. Electrophysiological comparison between sEPSPs and uEPSPs.
(A) Cumulative probability plot of all excitatory post-synaptic potentials amplitude. Inset, mean amplitude ± SEM of recorded uEPSPs and sEPSPs. (B) Cumulative probability plot of all

excitatory post-synaptic potentials 20-80 rise-time. Inset, mean rise-time ± SEM of recorded uEPSPs and sEPSPs. (C) Cumulative probability plot of all excitatory post-synaptic potentials decay tau. Inset, mean decay tau ± SEM of recorded uEPSPs and sEPSPs. (D) Cumulative probability plot of all excitatory post-synaptic currents amplitude. Inset, mean amplitude ± SEM of recorded uEPSCs and sEPSCs. Star indicate $p < 0.05$.

3.3 The co-existence of functional glutamatergic synapses on distinct subcellular locations

A series of studies from Dr. Kathryn Commons' lab investigating the glutamatergic innervation of the DRN with electron microscopy and array tomography found that glutamatergic inputs innervated both dendritic spines and shaft of DRN 5-HT neurons (Commons et al., 2005; Soiza-Reilly and Commons, 2011a, 2011b). Evidently, glutamatergic innervation suggests the presence of excitatory synapses on both dendritic structures (i.e., spines and shaft). However, these findings only demonstrate the presence of the pre-synaptic machinery require to form an excitatory synapse and does not prove it successfully gives rise to functional excitatory synapses. It led us to examine the co-existence of functional excitatory synapses on dendritic spines and the dendritic shaft of DRN 5-HT neurons.

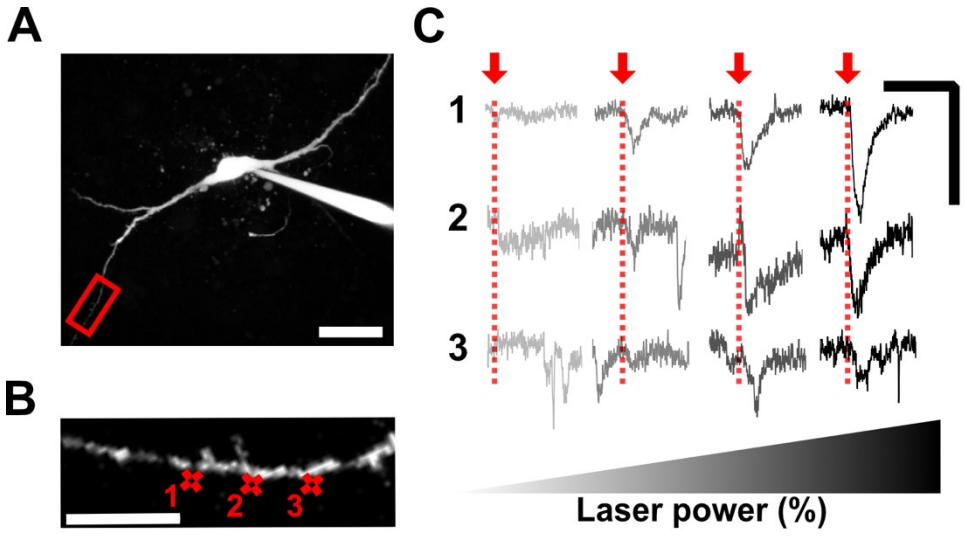

Figure 4. Dendritic Shaft Hotspot.
(A) Multi-photon image of a DRN 5-HT neuron with morphological marker Alexa 594 (scale bar; 25 µm). (B) High-magnification image of the dendritic segment marked by the red box (scale bar;

5 µm). Uncaging ROIs marked with red crosshairs. (C) Resulting excitatory post-synaptic currents (EPSCs) at putative shaft synapses (scale bar; 40 pA/20 msec). The red arrows represent the onset of the uncaging pulse. The dendritic ROI eliciting the largest uEPSC is considered as a current hotspot. The shading gradient is associated to the laser power used when stimulating the ROIs. Bottom, laser power scale ranging from 11% (lighter shade) to 33% (darker shade).

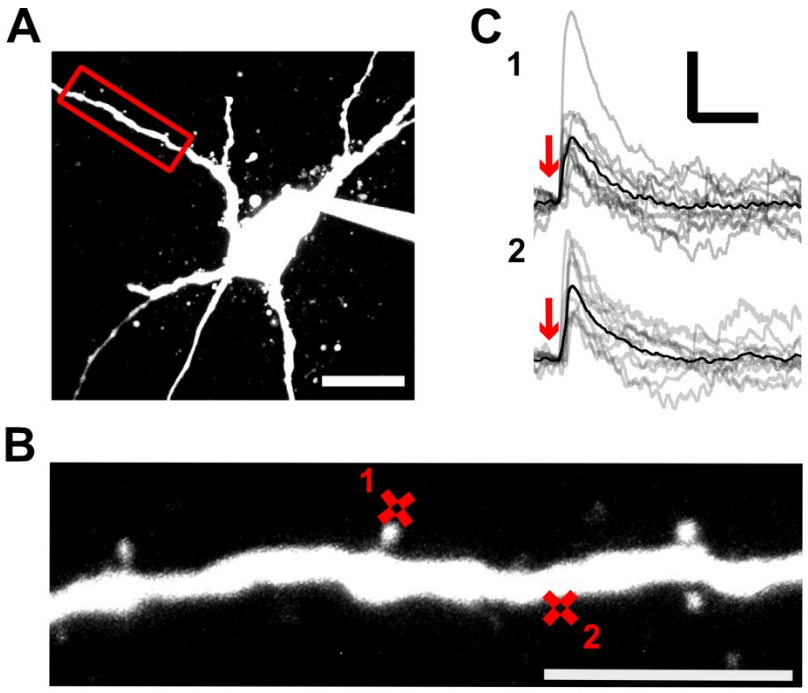

Figure 5. Presence of functional glutamatergic receptors on dendritic spines and dendritic shaft hotspots.
(A) Multi-photon image of a DRN 5-HT neuron with morphological marker Alexa 594 (scale bar; 20 µm). (B) High-magnification image of the dendritic segment marked by the red box (scale bar; 10 µm). Uncaging ROIs marked with red crosshairs. (C) All the traces of uncaging-evoked excitatory post-synaptic potentials (uEPSPs) elicited at dendritic spines (1; top) and all uEPSPs elicited at dendritic shaft hotspots (2; bottom) (scale bar; 1 mV/100 ms). The red arrows represent the onset of the uncaging pulse. The darker trace represents the mean uEPSP shape.

To reliably identify putative synapses located on the dendritic shaft, we used a protocol outlined in a recent study investigating the functional distinctions between spine and dendritic (i.e. shaft) synapses onto parvalbumin-positive interneuron in the mouse cortex (Sancho and Bloodgood, 2018) (Figure 4). The goal was to identify current "hotspots" on the dendritic shaft suggesting clustered expression of functional glutamatergic post-synaptic receptors. Following this method, we selected 3 region-of-interests (ROIs) on a dendritic segment free of spines (Figure

4B). We sequentially (i.e. 500 ms inter-pulse interval) uncaged at each ROI with increasingly higher laser power while recording uEPSCs in voltage clamp (-70mV) (Figure 4C). The ROI yielding the largest, time-locked, uEPSC was considered as a current hotspot. After establishing functional synaptic sites for shaft and spine synapses (Figure 5A-B), uEPSPs were measured by local glutamate uncaging for 27 individual ROIs in current clamp from 16 neurons and 13 mice (Figure 5C). Important to note, all ROIs were located at various depths, and thus, to account for the light-scattering properties of living brain slices, the laser power had to be adjusted according to the depth of the ROI. To ensure we consistently photolyze the same concentration of MIN-Glutamate across all ROIs, the intensity of the uncaging laser was tuned to generate a 15-20 pA AMPA-mediated EPSC at a holding potential of -70 mV, based on previously recorded spontaneous EPSC amplitude (Figure 3D). Next, we investigated whether spine and shaft synapses had a different electrical impact on the soma, by measuring uEPSPs kinetics. We found that the mean amplitude (Fig. 6A, Spine: 1.52 ± 0.269 mV, n = 16; Shaft: 1.23 ± 0.114 mV, n = 11; p = 0.3262, Student T-test), mean rise-time (Fig. 6B, Spine: 4.22 ± 0.419 ms, n = 16; Shaft: 4.58 ± 0.71 ms, n = 11; p = 0.6652, Student T-test), and mean decay tau (Fig. 6C , Spine: 48.11 ± 4.40 ms, n = 16; Shaft: 45.07 ± 4.95 ms, n = 11; p = 0.651, Student T-test) of uEPSPs, from the spines and shaft current hotspots, did not differ. Our results, taken together with the ultrastructural data from the Commons laboratory, demonstrate that DRN 5-HT neurons possess two structurally and morphologically distinct glutamatergic synapses, yet our cursory investigation showed that local activation of spine and shaft synapses did not appear to differently impact somatic membrane potential.

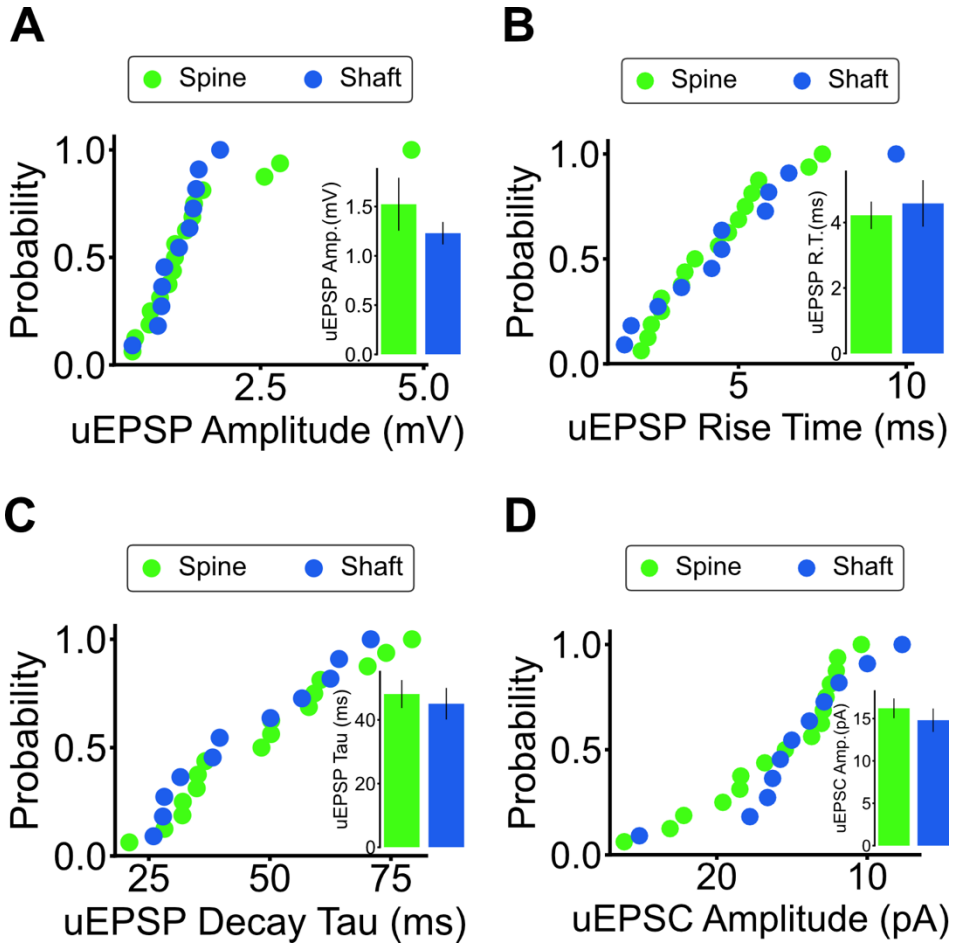

Figure 6. Comparison between dendritic spines and dendritic shaft hotspots.
(A) Cumulative probability plot of all uncaging-evoked excitatory post-synaptic potentials amplitude. Inset, mean amplitude ± SEM of recorded uEPSPs at spines and shaft hotspots. (B) Cumulative probability plot of all uncaging-evoked excitatory post-synaptic potentials 20-80 rise-time. Inset, mean rise-time ± SEM of recorded uEPSPs at spines and shaft hotspots. (C) Cumulative probability plot of all uncaging-evoked excitatory post-synaptic potentials decay tau. Inset, mean decay tau ± SEM of recorded uEPSPs at spines and shaft hotspots. (D) Cumulative probability plot of all uncaging-evoked excitatory post-synaptic currents amplitude. Inset, mean amplitude ± SEM of recorded uEPSCs at spines and shaft hotspots.

3.4 Local synaptic feature: AMPAR/NMDAR current ratios

To further investigate whether these two structurally different spine and shaft synapses were functionally different, we turned our attention to their subcellular glutamatergic receptor compositions. Since AMPA receptors (AMPARs) and NMDA receptors (NMDARs), and their current ratios, are decisive features of synaptic functions, we examined the AMPAR/NMDAR

current ratios at dendritic spines and dendritic shaft hotspots. Because of the temporally distinguishable kinetics of NMDAR and AMPAR (Béïque et al., 2006), we separately measured AMPAR- and NMDAR-mediated uEPSCs (Figure 7A). Although less precise than using a pharmacological approach by administration of a NMDAR antagonist (e.g., DL-AP5), this method allowed sampling over a much broader population of recordings. We found the AMPA/NMDA ratios did not differ between dendritic spines and shaft hotspots (Fig. 7B, Spine: 1.60 ± 0.126 n = 26; Shaft: 1.66 ± 0.216, n = 18; p = 0.7956, Student T-test), however, we uncovered an interesting synaptic feature. The AMPAR-mediated EPSCs, regardless of the synapse type (e.g. spine or shaft), was much higher than the NMDAR-mediated EPSCs resulting in the mean AMPAR/NMDAR current ratio to be well above 1. This important dendritic feature of DRN 5-HT neurons highlighted a significant disparity between the contributions of AMPAR and NMDAR to synaptic functions.

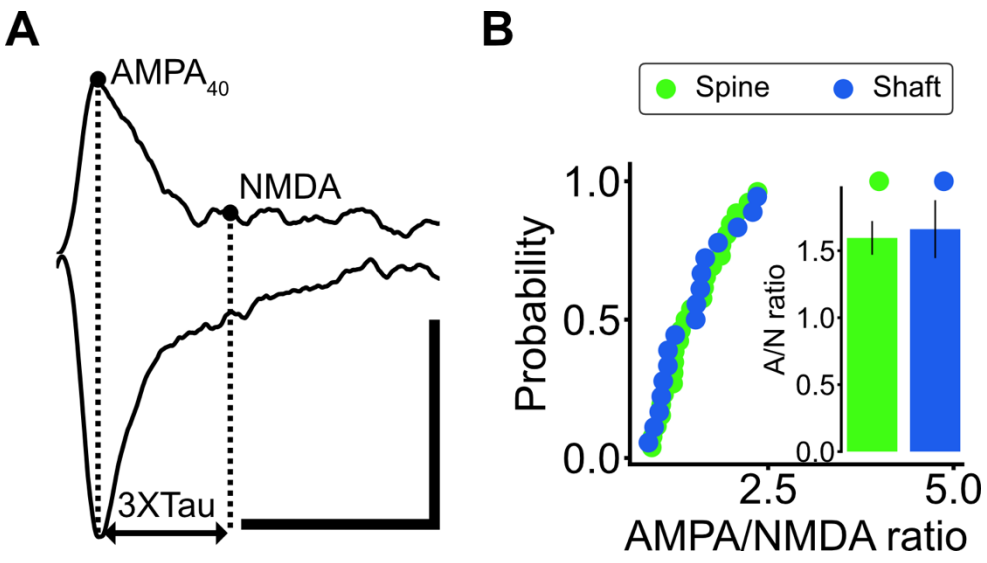

Figure 7. Subcellular receptor composition at dendritic spines and dendritic shaft hotspots.
(A) Voltage-clamp traces illustrating the method utilized to determine the AMPA NMDA ratio. Uncaging-evoked excitatory post-synaptic current (uEPSC) at a holding potential of -70 mV (bottom), and uEPSC at a holding potential of +40 mV (top) (scale bar; 20 pA/10 ms). *$AMPA_{40}$* marks the amplitude of the AMPA component at +40 mV. *NMDA* marks the amplitude of the NMDA component at a time when the AMPA component at -70 mV has decayed (~3x tau). (B)

Cumulative probability plot of all AMPA NMDA ratios. Inset, mean AMPA NMDA ratio ± SEM recorded at spines and shaft hotspots.

3.5 Reduced effects of Rall's concept of dendritic filtering in DRN 5-HT neurons

Dendritic morphology and the distribution of synaptic inputs along the dendritic arborization greatly influence neuronal input processing (Tran-Van-Minh et al., 2015). Wilfrid Rall's pioneering work uses a multi-compartmental equivalent circuit model to help inform how neuronal morphology, such as dendritic arborization, influenced synaptic integration in neurons. Rall's primary advancement considers dendrites as cylindrical electrical cables introducing the concept of dendritic filtering (Rall, 1967). Dendritic filtering occurs when each compartment allows current to leak across the membrane, resulting in the voltage in the next compartment to become progressively smaller and slower (Rall and Rinzel, 1974; Tran-Van-Minh et al., 2015). Dendritic filtering explains, in part, why more distal synaptic inputs result in smaller EPSPs recorded at the soma, comparatively to more proximal inputs (Spruston et al., 1994). Dendritic filtering is a simple mechanism by which a neuron can perform local computations. The current lack of knowledge on the computational abilities of DRN 5-HT neurons prompted us to investigate whether these neurons are endowed with such local input processing mechanism.

To observe the effect dendritic filtering would have on synaptic potentials as they propagated along the dendrite to the soma, we began by implementing two "Ball-and-Stick" models with NEURON (Hines and Carnevale, 2001). Using a computational approach allowed us to build a null framework to directly compare to subsequent experimental results. To ensure our models reflected the behaviour of DRN 5-HT neurons, we used morphological and electrophysiological features collected during our research (e.g., time constant, dendritic length, dendritic diameter). To focus on the behavior expected from a passive dendrite, we did not include any active dendritic conductance, furthermore, it is currently not known if 5-HT dendrites express

active conductance. In the first model, we built a simple neuron with a cylindrical cable-like dendrite demonstrating Rall's concept of dendritic filtering (Figure 8A). As expected, the proximal synaptic input had a significantly larger somatic depolarization than the distal input (Figure 8A). To address the gradual decrease in dendritic diameter we observed (Figure 1G), in the second model, we built a simple neuron with a tapered dendrite to match out morphological analysis of 5-HT neurons (Figure 8B). A change in diameter along the diameter leads in a variation in local input impedance. As such, variation in local input impedance caused by a neuron's dendritic architecture has the potential to counteract filtering by virtue of passive synaptic normalization (Jaffe and Carnevale, 1999). Thus, we felt it was paramount to capture this morphological feature of DRN 5-HT neuron in our computational experiments. The second model showed a decreased of the distance-dependent effect on somatic depolarization, however the somatic depolarization associated to the proximal input remained larger and faster than the distal input (Figure 8B). Based on our computational modeling we hypothesized that the simple dendritic arborization of 5-HT neurons was likely subject to dendritic filtering.

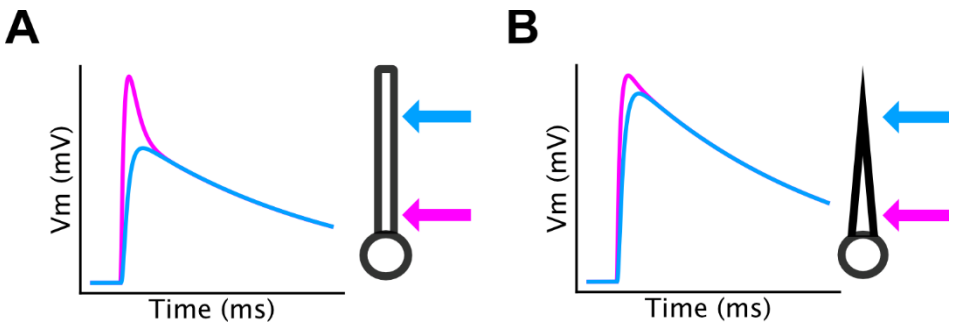

Figure 8. Ball-and-stick models.
(A) Graph representing the somatic depolarization in response to proximal synaptic input (pink) and distal synaptic input (blue) in a model depicting dendritic filtering. Inset, cylindrical ball-and-stick model schematic with colored arrow depicting the location of two synapses. (B) Graph representing the somatic depolarization in response to proximal synaptic input (pink) and distal synaptic input (blue) in a model depicting passive synaptic normalization. Inset, tapered ball-and-

stick model of a neuron with colored arrow depicting the location of two synapses. The proximal input and distal input were located 16 μm and 240 μm away from the soma, respectively.

To test our hypothesis, we used an experimental approach where we stimulated by uncaging a synapse located less than 50 μm away from the soma (i.e., proximal) and a synapse located more than 50 μm away from the soma (i.e., distal), and recorded their respective uEPSPs (Fig. 9A). To account for potential differences across dendrites, we only compared uEPSPs obtained from synapses located on the same dendrite. The example trace, generated from the ROIs depicted in Figure 9A, showed the absence of the dendritic filtering in this 5-HT dendrite. The distal uEPSP displayed significantly larger amplitude and faster kinetics than the proximal uEPSP (Figure 9B). After further investigation, the reduced effects of dendritic filtering, observed in Figure 9B, remained when we analyzed 8 other paired-uEPSPs from 8 different DRN 5-HT neurons. The amplitude of uEPSPs elicited near the soma were not significantly larger than the uEPSPs elicited at least 50 μm away from the soma (Figure 9C; Amplitude, < 50 μm: 1.23 ± 0.208, > 50 μm: 1.71 ± 0.401, $n = 9$, $p = 0.9727$; one-tail Paired Wilcoxon signed-rank test), and the rise time and decay time of proximal uEPSPs were not significantly faster than distal uEPSPs (Figure 9D-E; Rise-Time, < 50 μm: 4.43 ± 0.618, > 50 μm: 4.04 ± 0.579, $n = 9$, $p = 0.2731$; Decay Tau, < 50 μm: 45.9 ± 6.38, > 50 μm: 44.4 ± 5.39, $n = 9$; $p = 0.5831$; one-tail Paired Student t-test). Our results demonstrated that DRN 5-HT neurons, in general, did not exhibit the distance-dependent effects associated with dendritic filtering, perhaps reflecting the tapered distal dendritic morphology observed earlier, and providing a mechanism for apical and distal inputs to have equivalent access to the somatic spiking machinery. While still incomplete, our results nonetheless demonstrate the ability of the uncaging approach to provide a powerful means to fully parametrize the spatial and temporal presentations of inputs onto 5-HT neurons and to highlight their

integrative features. Furthermore, our findings demonstrated that synaptic integration in DRN 5-HT neurons were not completely captured by our simple computational models.

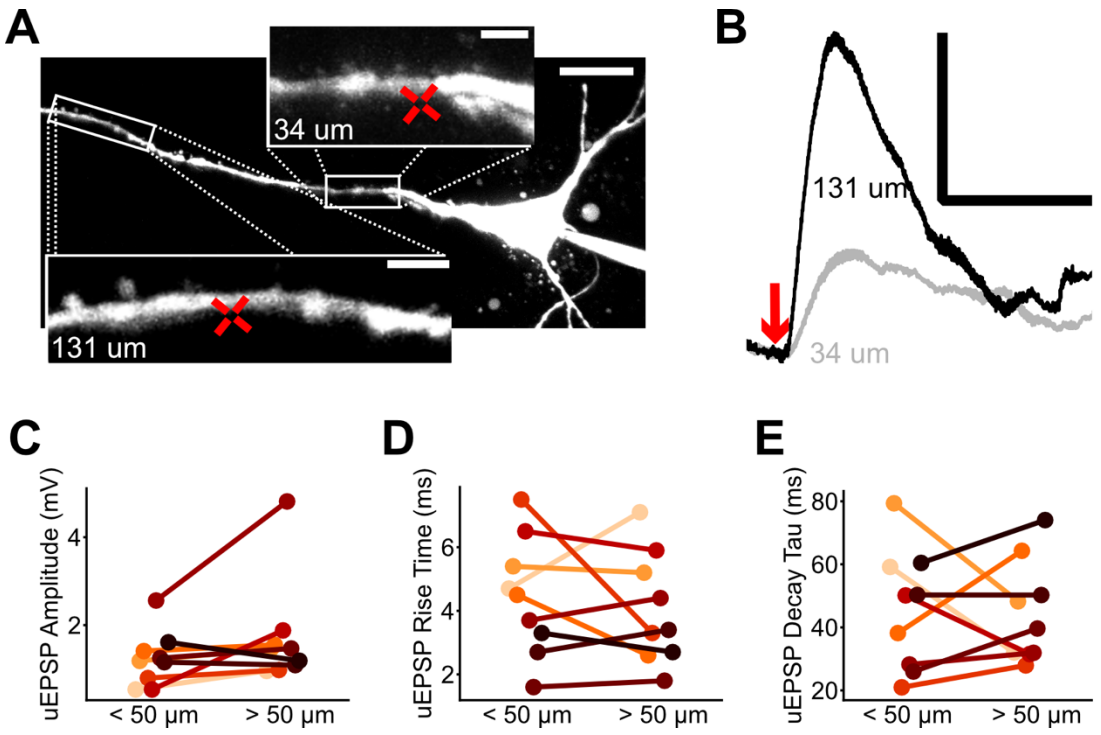

Figure 9. Distance-dependent effect on somatic excitatory post-synaptic potentials.
(A) Multi-photon image of a DRN 5-HT neuron with morphological marker Alexa 594 (scale bar; 25 µm). Top, high-magnification image of the dendritic segment marked by the white box (scale bar; 5 µm). Bottom, high-magnification image of the dendritic segment marked by white box (scale bar; 5 µm). The red crosshairs indicate the location of the uncaging ROIs. The corresponding distance from the soma is indicated on the lower left side. (B) The resulting uEPSPs obtained following the activation of the two shaft hotspots illustrated in panel A (scale bar; 1 mV/40 ms). (C-E) Graphs illustrating the uEPSP parameters obtained from proximal (first 50 µm) and distal (remaining length) ROIs located on the same dendrite.

4. Discussion

4.1 Co-Existence of Structurally and Morphologically Distinct Synapses

Several studies have now observed that specific long-range inputs preferentially target anatomically and/or molecularly segregated sub-population of 5-HT neurons (Huang et al., 2019;

Okaty et al., 2020; Ren et al., 2018, 2019). Probing individual synapses, using multi-photon microscopy and glutamate uncaging, we found evidence of functional glutamatergic synapses on both the dendritic spines and the dendritic shaft of 5-HT neurons. The co-existence of two structurally and morphologically distinct putative glutamatergic synapses offers a scenario where specific DRN inputs can preferentially target different subcellular locations across the dendritic arbor. While, no evidence, so far, can confirm if spine and shaft synapses are receiving inputs from separate brain regions, the co-localization of two distinct synaptic compartments provides promising preliminary data.

Previous studies also provided additional supporting evidence for the possible role of dendritic domains in processing local inputs. For example, an ultrastructural imaging study, conducted in rats, revealed two populations of glutamatergic inputs primarily project to DRN 5-HT neurons. They are distinguished based on the type of vesicular glutamate transporter (vGlut) expressed in the afferent axon (Commons et al., 2005). The study found axons containing the type 1 vesicular glutamate transporter (vGlut1) mostly innervated distal (small-caliber) dendrites and dendritic spines. While the type 2 vesicular glutamate transporter (vGlut2)-containing axons contacted proximal (large-caliber) dendritic shafts (Commons et al., 2005). This data provides supporting evidence of the presence of preferential synaptic connection from two populations of inputs to distinct structural and morphological regions of the dendrite. What makes this finding even more compelling is additional research on the pattern of expression of vGluts that has demonstrated vGlut1 expression to predominate in cortical regions (e.g., prefrontal cortex), whereas vGlut2 is widely expressed in subcortical areas (e.g., lateral habenula) (Fremeau et al., 2001; Kaneko and Fujiyama, 2002). Taken together, these findings are building a strong case

supporting a microscale circuitry, in DRN 5-HT neurons, where cortical and subcortical afferent axons preferentially make contact with spine and shaft synapses, respectively.

For the scope of this study, an important caveat remains since the ultrastructural findings outlined above were found in rats. Therefore, we must remain cautious in inferring similarities between the dendritic features of the rat and mouse DRNs. Nevertheless, our survey of the mouse DRN confirms two hallmark dendritic features present in both rodent species: (1) the tapering regime of primary dendrites (Figure 1G), and (2) the higher density of spines on distal dendrites (Figure 1H). While the ultrastructural study from the Commons' laboratory found the presence of putative synapses on dendritic spines and the dendrite shaft, our *in-vitro* electrophysiological work confirmed those structurally and morphologically distinct subcellular locations also housed functional glutamatergic receptors, and together these results provide strong evidence of the co-existence of two distinct types of glutamatergic synapses. The preferential microscale pattern of connectivity previously observed, between vGlut1- and vGlut2-containing axons onto 5-HT dendrites, however, remains to be verified in the mouse DRN. Interestingly, recent advances in viral vector strategies have provided new alternative methods to electron microscopy for the mapping of inputs on single dendrites. Now, some viral tools are able to map region-specific inputs onto a single neuron. For instance, the mammalian GFP reconstitution across synaptic partners (mGRASP) technique can selectively target a long-range input by first injecting the projecting region-of-interest with a non Cre-dependent AAV and sequentially injecting a Cre-dependent AAV in a Cre (cre/+) mouse (Druckmann et al., 2014; Feng et al., 2014; Kim et al., 2012; Song et al., 2018). Resulting in the conditional expression of a green fluorescent protein (GFP) at the point of contact (i.e., the synapse) between the afferent axons and the post-synaptic density (PSD), which can be visualization using fluorescence imaging. While still promising, I unfortunately was not

able to satisfactorily develop this method for glutamatergic inputs to the raphe. The concept of preferential pattern of glutamatergic inputs being present at various levels of organization (i.e., sub-populations of synapses and sub-population of neurons) represents a fascinating computational mechanism. One potentially being leverage by the DRN to efficiently perform layers of simple and complex computations on its various many diverse classes of inputs.

4.2 Synaptic AMPA-to-NMDA Receptor Ratio

The existence of different morphological and structural dendritic domains provides a starting point for the organization of different input streams in 5-HT neurons by creating unique intersections across the dendritic arbor where specific synaptic inputs converge. Next, we explored if spine and shaft synapses were equipped with mechanisms specialized for processing the features for their respective inputs. We started by measuring the AMPA to NMDA ratios on spine and shaft synapses. Changes in synaptic AMPA to NMDA receptor ratio have previously been showed to contribute to differences in processing mechanism between dendritic compartments (Jang et al., 2015; Lafourcade et al., 2022). Although, no significant differences in the synaptic ratio of ionotropic glutamate receptors between spine and shaft synapses were found. Our results highlighted that most 5-HT synapses, located on both shaft and spine, displayed high synaptic AMPA to NMDA receptor ratio (Figure 7B). The significance of this finding, in shaping the DRN 5-HT synaptic landscape, becomes particularly evident when taken together with studies on glutamate receptor subunits and local dendritic input processing.

4.2.1 Glutamate Receptor Subunits in 5-HT Neurons

AMPARs and NMDARs are made up of four major subunits that form heteromeric tetrameric complexes (Traynelis et al., 2010). The four homologous core subunits for AMPARs are known as GluA1-4 and can formed both hetero- and homomers giving rise to a wide range of different receptor forms. The hippocampus, for instance, has been showed to house GluA1/2 and GluA2/3 heteromers as well as GluA1 homomers (Huganir and Nicoll, 2013). The NMDARs, on the other hand, require the assembly of two GluN1 and two GluN2 subunits (i.e., GluN2A-D), or a combination of GluN2 and GluN3 subunits (Pachernegg et al., 2012; Traynelis et al., 2010). Each of these receptor subunits are subject to conformational changes, often through phosphorylation, which may influence a receptor's ligand binding, activation, and desensitization (Huganir and Nicoll, 2013; Pachernegg et al., 2012; Traynelis et al., 2010). The expression of specific glutamate receptor subunits in 5-HT neurons is likely to play an important role in what we have observed with the synaptic glutamatergic receptor current ratio. A previous study, based on the Allen Brain Institute's Mouse Atlas, provides a detailed summary the expression pattern and level of glutamate receptor subunits in the DRN 5-HT neurons (Soiza-Reilly and Commons, 2011a). Interestingly, the analysis reveals that GluN1 and GluN3A expression levels are higher than other subunits in the DRN (Soiza-Reilly and Commons, 2011a). Given that the co-expression of GluN1/GluN3 alone only forms glycine-activated receptors (Pachernegg et al., 2012; Traynelis et al., 2010). It suggests that glutamate-sensitive NMDA receptor complexes in 5-HT neurons are formed by a combination of GluN1/GluN2/GluN3.

The current research on GluN3 subunit-containing NMDA receptors has found that this specific subunit combination yields lower glutamate-activated current amplitudes when compared to the classical GluN1 and GluN2 receptor complex (Pachernegg et al., 2012; Traynelis et al.,

2010). The high expression of GluN3 subunits, in DRN 5-HT neurons, supports what we observed experimentally with the dominance of the synaptic AMPAR-mediated conductance over NMDAR-mediated current. Studies comparing the co-expression of GluN3 with GluN1 and GluN2 to the classical GluN1/GluN2-containing NMDARs also found GluN3 expression reduce the Mg^{2+} sensitivity and Ca^{2+} permeability in GluN1/GluN2/GluN3-containing receptors (Pachernegg et al., 2012). These findings can explain why, in our study, we were unsuccessful in recording NMDAR-mediated calcium signals following uncaging events. The decreased current amplitude and Ca^{2+} permeability linked the expression of the GluN3 serves has been hypothesized to reflect a neuroprotective/synaptic brake mechanisms against synaptic bombardment (Pachernegg et al., 2012). This mechanism adds to other neuroprotective mechanisms, such as the I_a potassium current-induced suppression of response to transient excitatory inputs (Harkin *et al.,* 2021), 5-HT_{1A} receptor-mediated inhibition upon burst synchronous spiking (Lynn *et al.*, unpublished), and target-specific modulation of the excitatory inputs via endocannabinoids signaling (Geddes et al., 2016) already characterized by our laboratory. Moreover, deletion and overexpression of the GluN3 subunit has been shown to respectively increase and decrease spine density in cortical neurons (Pachernegg et al., 2012). The link between GluN3 expression and the dendritic morphology of 5-HT neurons, provides yet another example of the potential impact specific glutamatergic receptor subunit expression has on the synaptic landscape of the DRN. Based on the literature and our experimental findings, there is a conceivable link between the expression levels of the GluN3 glutamate receptor subunits, the synaptic AMPA-to-NMDA receptor ratio, and the spine density in 5-HT neuron. Thereupon, future experiments aim at confirming the presence GluN3A-containing NMDARs and define their role in the DRN 5-HT system is top of mind. However, the lack of specific antagonists, or inducible transgenic strategies,

to target the GluN3 subunit presents a significant roadblock for future research aim to experimentally characterize the repercussion this glutamate receptor subunit on the dendritic properties of DRN 5-HT neurons.

4.2.1 Local Input Processing in 5-HT Neurons

No studies have yet to investigate nonlinear dendritic integration in 5-HT neurons. The dendritic morphology of 5-HT cells presents a picture where sublinear, linear, and supralinear dendritic integration regime is possible. Studies on aspiny dendrites have shown a lack of supralinear mechanisms, limiting these neurons to only linear or even sublinear integration (Tran-Van-Minh et al., 2016). On the other hand, numerous studies on spiny dendrites have shown the integration of excitatory inputs is primarily done through supralinear dendritic processing (Branco and Häusser, 2011; Larkum, 2013, 2013; Major et al., 2013; Takahashi et al., 2016). Positioned in between aspiny and spiny dendrites, sparsely spiny dendrites have shown the ability to access both supralinear and sublinear integrative strategies (Sancho and Bloodgood, 2018), offering some provisional evidence to support a similar framework in 5-HT neurons. Moreover, the thin caliber of 5-HT dendrites (Figure 1G) provides a favorable environment for NMDA-mediated dendritic spikes (NMDA spikes) believed to be the principal nonlinear neuronal operations used in thin spiny dendrites (Branco and Häusser, 2011; Larkum, 2013; Major et al., 2013).

The presence of a high synaptic AMPA to NMDA receptor ratio across 5-HT excitatory synapses, however, stands as a strong biophysical argument against NMDAR-mediated supralinearity in 5-HT dendrites. Upon synaptic stimulation of a 5-HT synapse, the large AMPA component produces a large voltage kick, which reaches the synaptic reversal potential while the NMDA conductance remains relatively low (Major et al., 2013). Under this electrophysical

scenario, NMDARs are hindered from undergoing the internal conformational changes necessary to relieve the magnesium block and reach maximal conductance (Major et al., 2013). Even if the input is increased, the maximum response only grows in a graded manner, and never triggering a sharp, all-or-nothing, voltage step, known as a dendritic spike (Major et al., 2013). This represents a significant advancement in the exploration of the local dendritic input processing of 5-HT cells. Although, the presence of other nonlinear mechanisms, such as fast local Na^+ spikes and long-lasting global Ca^{2+} spikes (Tran-Van-Minh et al., 2015), has yet to be ruled out, the lack of NMDA spikes strongly suggests that 5-HT dendrites primarily exhibit linear integration of their excitatory inputs. This insensitivity of 5-HT dendrites to specific spatiotemporal input-pattern does not, however, exclude nonlinear processing via the amplification backpropagating action potentials (bAPs) by coincidence detection (Stuart and Häusser, 2001). We know that bAPs are present in 5-HT dendrites (Suppl. Fig 1.), amplification of backpropagating action potentials by EPSPs provides a sensitive mechanism linking the global activity of the neuron to activity of specific sets of synaptic inputs (Stuart and Häusser, 2001). This mechanism would allow 5-HT cells to selectively detect inputs contributing to the generation of synchronous network activity. Future work studying dendritic subthreshold input-output (sI/O) relationship will be necessary to identify the different classes of dendritic operations (linear, sublinear, supralinear) present in 5-HT dendrites.

4.3 Reduced Dendritic Filtering in DRN 5-HT Neurons

A simple, yet effective, way for neurons to linearly process spatially divergent inputs across the dendritic tree is by prioritizing the resulting local synaptic potentials based on their distance from their soma. Known as dendritic filtering, this mechanism, characterized more than 50 years ago

(Rall, 1967), transforms local electrical inputs in a distance-dependant manner as it travels down a dendritic branch (Rall and Rinzel, 1974; Tran-Van-Minh et al., 2016). In our study, we set out to investigate the outcome of this simple scenario; will a 5-HT neuron differentiate between two inputs spatially distributed along the same dendritic branch? Rall's pioneer work suggests that through the effect of dendritic filtering a neuron can discriminate a distal input from a proximal input (Rall and Rinzel, 1974). Our computational work reinforced the potential role of dendritic filtration when tested in an electrotonically passive, serotonin-like, ball-and-stick model (Figure 8A). In a physiological environment, however, our experimental results gave rise to a much more diverse set of outcomes (Figure 9C-D). In one case the distal input displayed a significant boosting in comparison to the proximal input (Figure 9B). Directly counteracting the anticipated outcome of dendritic filtering. As illustrated in the computational model depicting passive synaptic normalization (Figure 8B), a change in local input impedance due to a tapering dendrite cannot completely account for such an amplification in distally evoked input and hitting that 5-HT dendrites are active compartments. However, we are unable, at this time, to identify the ionic conductance responsible for this boosting. Our preliminary findings suggest that NMDAR-mediated boosting is unlikely, due to the high synaptic AMPA-to-NMDA ratio. One possible scenario is a distance-dependent increase in AMPAR expression, known as distance-dependent conductance scaling, a mechanism used by hippocampal CA1 neurons to minimize the influence of distance on synaptic efficacy (Andrásfalvy and Magee, 2001; Smith et al., 2003; Nicholson et al., 2006). Our results reaffirm that the local input processing rules of 5-HT cells are complex and cannot simply be categorized as linear. Future works focusing on location of the inputs (i.e., distance from the cell body), dendritic branching patterns, and parent/daughter dendrite caliber

ratios (for impedance mismatch analysis along the electrotonic path) will be paramount to provide the first comprehensive description of the dynamic behavior of 5-HT neurons' dendrites.

4.4 Conclusion

Our understanding of synaptic integration has been largely shaped by the prototypical morphology of densely spiny neurons, at times, overlooking the neuronal strategies employed by other neurons with few spines (i.e., sparsely spiny) or no spines (i.e., aspiny). Which, in turn, as resulted in a scarce and incomplete survey of the dendritic features of DRN 5-HT neurons. While synaptic contact onto dendritic spines is agreeably very favorable for both moment-to-moment computation and learning-related plasticity in the mammalian brain (Yuste, 2011), the remaining available "spineless" membrane on the dendrite (i.e., the dendritic shaft) also represents an adequate, and beneficial, mediator for excitatory connections in the CNS (Goldberg et al., 2003; Sancho and Bloodgood, 2018; Tran-Van-Minh et al., 2016). In this study, we set out to explore the dendritic landscape of DRN 5-HT neurons, in hopes to shed light on the dendritic operations responsible for the transformation of long-range inputs to DRN into a cohesive serotonin output. Using whole-cell electrophysiology recordings, in combination with multi-photon glutamate uncaging, we have identifying co-existing morphologically and structurally distinct synaptic sites located on the same dendrite with functionally large AMPAR- and small NMDAR-mediated conductance. Although, our initial findings have not identified specific local dendritic operations, they have provided valuable insights on local rules that governs how synaptic inputs to the DRN are being processed. to ultimately confer 5-HT neurons their unique coding features. This framework will greatly enrich our ongoing effort to characterize the unique coding features of 5-HT neurons, and to understand the role of serotonin in behavior, in health and disease.

References

Andrásfalvy, B.K., and Magee, J.C. (2001). Distance-Dependent Increase in AMPA Receptor Number in the Dendrites of Adult Hippocampal CA1 Pyramidal Neurons. The Journal of Neuroscience 21, 9151–9159. 10.1523/JNEUROSCI.21-23-09151.2001.

Baker, K.G., Halliday, G.M., and Törk, I. (1990). Cytoarchitecture of the human dorsal raphe nucleus: HUMAN DORSAL RAPHE. J. Comp. Neurol. *301*, 147–161. https://doi.org/10.1002/cne.903010202.

Baker, K.G., Halliday, G.M., Halasz, P., Hornung, J.-P., Geffen, L.B., Cotton, R.G.H., and Törk, I. (1991). Cytoarchitecture of serotonin-synthesizing neurons in the pontine tegmentum of the human brain: SEROTONERGIC NEURONS IN HUMAN PONS. Synapse *7*, 301–320. https://doi.org/10.1002/syn.890070407.

Béïque, J.-C., Lin, D.-T., Kang, M.-G., Aizawa, H., Takamiya, K., and Huganir, R.L. (2006). Synapse-specific regulation of AMPA receptor function by PSD-95. Proc. Natl. Acad. Sci. *103*, 19535–19540. https://doi.org/10.1073/pnas.0608492103.

Béïque, J.-C., Imad, M., Mladenovic, L., Gingrich, J.A., and Andrade, R. (2007). Mechanism of the 5-hydroxytryptamine 2A receptor-mediated facilitation of synaptic activity in prefrontal cortex. Proc. Natl. Acad. Sci. *104*, 9870–9875. https://doi.org/10.1073/pnas.0700436104.

Béïque, J.-C., Na, Y., Kuhl, D., Worley, P.F., and Huganir, R.L. (2011). Arc-dependent synapse-specific homeostatic plasticity. Proc. Natl. Acad. Sci. *108*, 816–821. https://doi.org/10.1073/pnas.1017914108.

Benda, J., Longtin, A., and Maler, L. (2006). A Synchronization-Desynchronization Code for Natural Communication Signals. Neuron *52*, 347–358. https://doi.org/10.1016/j.neuron.2006.08.008.

Branco, T., and Häusser, M. (2011). Synaptic Integration Gradients in Single Cortical Pyramidal Cell Dendrites. Neuron *69*, 885–892. https://doi.org/10.1016/j.neuron.2011.02.006.

Chacron, M.J., and Bastian, J. (2008). Population Coding by Electrosensory Neurons. J. Neurophysiol. *99*, 1825–1835. https://doi.org/10.1152/jn.01266.2007.

Cohen, J.Y., Amoroso, M.W., and Uchida, N. (2015). Serotonergic neurons signal reward and punishment on multiple timescales. ELife *4*. https://doi.org/10.7554/eLife.06346.

Commons, K.G., Beck, S.G., and Bey, V.W. (2005). Two populations of glutamatergic axons in the rat dorsal raphe nucleus defined by the vesicular glutamate transporters 1 and 2. Eur. J. Neurosci. *21*, 1577–1586. https://doi.org/10.1111/j.1460-9568.2005.03991.x.

Correia, P.A., Lottem, E., Banerjee, D., Machado, A.S., Carey, M.R., and Mainen, Z.F. (2017). Transient inhibition and long-term facilitation of locomotion by phasic optogenetic activation of serotonin neurons. ELife *6*. https://doi.org/10.7554/eLife.20975.

Dahlström, A., and Fuxe, K. (1964). Localization of monoamines in the lower brain stem. Experientia *20*, 398–399. https://doi.org/10.1007/BF02147990.

Druckmann, S., Feng, L., Lee, B., Yook, C., Zhao, T., Magee, J.C., and Kim, J. (2014). Structured Synaptic Connectivity between Hippocampal Regions. Neuron *81*, 629–640. https://doi.org/10.1016/j.neuron.2013.11.026.

Edmonds, B., Gibb, A.J., and Colquhoun, D. (1995). Mechanisms of Activation of Glutamate Receptors and the Time Course of Excitatory Synaptic Currents. 25. .

Ellis-Davies, G.C.R. (2019). Two-Photon Uncaging of Glutamate. Front. Synaptic Neurosci. *10*. https://doi.org/10.3389/fnsyn.2018.00048.

Fairhall, A.L., Lewen, G.D., and Bialek, W. (2001). Efficiency and ambiguity in an adaptive neural code. *412*, 6. .

Feng, L., Kwon, O., Lee, B., Oh, W.C., and Kim, J. (2014). Using mammalian GFP reconstitution across synaptic partners (mGRASP) to map synaptic connectivity in the mouse brain. Nat. Protoc. *9*, 2425–2437. https://doi.org/10.1038/nprot.2014.166.

Fernandez, S.P., Cauli, B., Cabezas, C., Muzerelle, A., Poncer, J.-C., and Gaspar, P. (2016). Multiscale single-cell analysis reveals unique phenotypes of raphe 5-HT neurons projecting to the forebrain. Brain Struct. Funct. *221*, 4007–4025. https://doi.org/10.1007/s00429-015-1142-4.

Fonseca, M.S., Murakami, M., and Mainen, Z.F. (2015). Activation of Dorsal Raphe Serotonergic Neurons Promotes Waiting but Is Not Reinforcing. Curr. Biol. *25*, 306–315. https://doi.org/10.1016/j.cub.2014.12.002.

Fremeau, R.T., Troyer, M.D., Pahner, I., Nygaard, G.O., Tran, C.H., Reimer, R.J., Bellocchio, E.E., Fortin, D., Storm-Mathisen, J., and Edwards, R.H. (2001). The Expression of Vesicular Glutamate Transporters Defines Two Classes of Excitatory Synapse. Neuron *31*, 247–260. https://doi.org/10.1016/S0896-6273(01)00344-0.

Geddes, S.D., Assadzada, S., Sokolovski, A., Bergeron, R., Haj-Dahmane, S., and Béïque, J.-C. (2015). Time-dependent modulation of glutamate synapses onto 5-HT neurons by antidepressant treatment. Neuropharmacology *95*, 130–143. https://doi.org/10.1016/j.neuropharm.2015.02.027.

Geddes, S.D., Assadzada, S., Lemelin, D., Sokolovski, A., Bergeron, R., Haj-Dahmane, S., and Béïque, J.-C. (2016). Target-specific modulation of the descending prefrontal cortex inputs to the dorsal raphe nucleus by cannabinoids. Proc. Natl. Acad. Sci. *113*, 5429–5434. https://doi.org/10.1073/pnas.1522754113.

Harkin, E.F., Payeur, A., Lynn, M.B., Boucher, J.-F., Caya-Bissonnette, L., Cyr, D., Stewart, C., Longtin, A., Naud, R., and Béïque, J.-C. (2021). Temporal derivative computation in the dorsal raphe network revealed by an experimentally-driven augmented integrate-and-fire modeling framework. bioRxiv. 10.1101/2021.06.25.449907.

Hines, M.L., and Carnevale, N.T. (2001). Neuron: A Tool for Neuroscientists. The Neuroscientist *7*, 123–135. https://doi.org/10.1177/107385840100700207.

Huang, K.W., Ochandarena, N.E., Philson, A.C., Hyun, M., Birnbaum, J.E., Cicconet, M., and Sabatini, B.L. (2019). Molecular and anatomical organization of the dorsal raphe nucleus. 34. .

Huganir, R.L., and Nicoll, R.A. (2013). AMPARs and Synaptic Plasticity: The Last 25 Years. Neuron *80*, 704–717. https://doi.org/10.1016/j.neuron.2013.10.025.

Iigaya, K., Fonseca, M.S., Murakami, M., Mainen, Z.F., and Dayan, P. (2018). An effect of serotonergic stimulation on learning rates for rewards apparent after long intertrial intervals. Nat. Commun. *9*. https://doi.org/10.1038/s41467-018-04840-2.

Ishimura, K., Takeuchi, Y., Fujiwara, K., Tominaga, M., Yoshioka, H., and Sawada, T. (1988). Quantitative analysis of the distribution of serotonin-immunoreactive cell bodies in the mouse brain. Neurosci. Lett. *91*, 265–270. https://doi.org/10.1016/0304-3940(88)90691-X.

Jacobs, B.L., and Azmitia, E.C. (1992). Structure and function of the brain serotonin system. Physiol. Rev. *72*, 165–229. https://doi.org/10.1152/physrev.1992.72.1.165.

Jaffe, D.B., and Carnevale, N.T. (1999). Passive Normalization of Synaptic Integration Influenced by Dendritic Architecture. J. Neurophysiol. *82*, 3268–3285. https://doi.org/10.1152/jn.1999.82.6.3268.

Jain, V., Murphy-Baum, B.L., deRosenroll, G., Sethuramanujam, S., Delsey, M., Delaney, K.R., and Awatramani, G.B. (2020). The functional organization of excitation and inhibition in the dendrites of mouse direction-selective ganglion cells. ELife *9*, e52949. https://doi.org/10.7554/eLife.52949.

Jang, M., Um, K.B., Jang, J., Kim, H.J., Cho, H., Chung, S., and Park, M.K. (2015). Coexistence of glutamatergic spine synapses and shaft synapses in substantia nigra dopamine neurons. Sci. Rep. *5*. https://doi.org/10.1038/srep14773.

Jonas, P., and Spruston, N. (1994). Mechanisms shaping glutamate-mediated excitatory postsynaptic currents in the CNS. Curr. Opin. Neurobiol. *4*, 366–372. https://doi.org/10.1016/0959-4388(94)90098-1.

Jones, E., Oliphant, T., and Peterson, P. (2001). SciPy: Open Source Scientific Tools for Python.

Kaneko, T., and Fujiyama, F. (2002). Complementary distribution of vesicular glutamate transporters in the central nervous system. Neurosci. Res. *42*, 243–250. https://doi.org/10.1016/S0168-0102(02)00009-3.

Kim, J., Zhao, T., Petralia, R.S., Yu, Y., Peng, H., Myers, E., and Magee, J.C. (2012). mGRASP enables mapping mammalian synaptic connectivity with light microscopy. Nat. Methods *9*, 96–102. https://doi.org/10.1038/nmeth.1784.

Koch, C., Poggio, T., and Torre, V. (1983). Nonlinear interactions in a dendritic tree: localization, timing, and role in information processing. Proc. Natl. Acad. Sci. *80*, 2799–2802. https://doi.org/10.1073/pnas.80.9.2799.

Lafourcade, M., van der Goes, M.-S.H., Vardalaki, D., Brown, N.J., Voigts, J., Yun, D.H., Kim, M.E., Ku, T., and Harnett, M.T. (2022). Differential dendritic integration of long-range inputs in association cortex via subcellular changes in synaptic AMPA-to-NMDA receptor ratio. Neuron *110*, 1532-1546.e4. https://doi.org/10.1016/j.neuron.2022.01.025.

Larkum, M. (2013). A cellular mechanism for cortical associations: an organizing principle for the cerebral cortex. Trends Neurosci. *36*, 141–151. https://doi.org/10.1016/j.tins.2012.11.006.

Larkum, M.E., Nevian, T., Sandler, M., Polsky, A., and Schiller, J. (2009). Synaptic Integration in Tuft Dendrites of Layer 5 Pyramidal Neurons: A New Unifying Principle. Science *325*, 756–760. https://doi.org/10.1126/science.1171958.

Lee, K.F.H., Soares, C., Thivierge, J.-P., and Béïque, J.-C. (2016). Correlated Synaptic Inputs Drive Dendritic Calcium Amplification and Cooperative Plasticity during Clustered Synapse Development. Neuron *89*, 784–799. https://doi.org/10.1016/j.neuron.2016.01.012.

Li, Y., Zhong, W., Wang, D., Feng, Q., Liu, Z., Zhou, J., Jia, C., Hu, F., Zeng, J., Guo, Q., et al. (2016). Serotonin neurons in the dorsal raphe nucleus encode reward signals. Nat. Commun. *7*. https://doi.org/10.1038/ncomms10503.

Li, Y.-Q., Li, H., Kaneko, T., and Mizuno, N. (2001). Morphological features and electrophysiological properties of serotonergic and non-serotonergic projection neurons in the dorsal raphe nucleus: An intracellular recording and labeling study in rat brain slices. Brain Res. 9.

London, M., and Häusser, M. (2005). DENDRITIC COMPUTATION. 32.

Lottem, E., Banerjee, D., Vertechi, P., Sarra, D., Lohuis, M. oude, and Mainen, Z.F. (2018). Activation of serotonin neurons promotes active persistence in a probabilistic foraging task. Nat. Commun. *9*. https://doi.org/10.1038/s41467-018-03438-y.

Luo, M., Li, Y., and Zhong, W. (2016). Do dorsal raphe 5-HT neurons encode “beneficialness”? Neurobiol. Learn. Mem. *135*, 40–49. https://doi.org/10.1016/j.nlm.2016.08.008.

Major, G., Larkum, M.E., and Schiller, J. (2013). Active Properties of Neocortical Pyramidal Neuron Dendrites. Annu. Rev. Neurosci. *36*, 1–24. https://doi.org/10.1146/annurev-neuro-062111-150343.

Marcinkiewcz, C.A., Mazzone, C.M., D’Agostino, G., Halladay, L.R., Hardaway, J.A., DiBerto, J.F., Navarro, M., Burnham, N., Cristiano, C., Dorrier, C.E., et al. (2016). Serotonin engages an anxiety and fear-promoting circuit in the extended amygdala. Nature *537*, 97–101. https://doi.org/10.1038/nature19318.

Matias, S., Lottem, E., Dugué, G.P., and Mainen, Z.F. (2017). Activity patterns of serotonin neurons underlying cognitive flexibility. ELife *6*. https://doi.org/10.7554/eLife.20552.

Matsuzaki, M., Ellis-Davies, G.C.R., Nemoto, T., Miyashita, Y., Iino, M., and Kasai, H. (2001). Dendritic spine geometry is critical for AMPA receptor expression in hippocampal CA1 pyramidal neurons. Nat. Neurosci. *4*, 1086–1092. https://doi.org/10.1038/nn736.

Miyazaki, K., Miyazaki, K.W., Yamanaka, A., Tokuda, T., Tanaka, K.F., and Doya, K. (2018). Reward probability and timing uncertainty alter the effect of dorsal raphe serotonin neurons on patience. Nat. Commun. *9*. https://doi.org/10.1038/s41467-018-04496-y.

Miyazaki, K.W., Miyazaki, K., Tanaka, K.F., Yamanaka, A., Takahashi, A., Tabuchi, S., and Doya, K. (2014). Optogenetic Activation of Dorsal Raphe Serotonin Neurons Enhances Patience for Future Rewards. Curr. Biol. *24*, 2033–2040. https://doi.org/10.1016/j.cub.2014.07.041.

Naud, R., and Sprekeler, H. (2018). Sparse bursts optimize information transmission in a multiplexed neural code. Proc. Natl. Acad. Sci. *115*, E6329–E6338. https://doi.org/10.1073/pnas.1720995115.

Nicholson, D.A., Trana, R., Katz, Y., Kath, W.L., Spruston, N., and Geinisman, Y. (2006). Distance-Dependent Differences in Synapse Number and AMPA Receptor Expression in Hippocampal CA1 Pyramidal Neurons. Neuron 50, 431–442. 10.1016/j.neuron.2006.03.022.

Ogawa, S.K., Cohen, J.Y., Hwang, D., Uchida, N., and Watabe-Uchida, M. (2014). Organization of Monosynaptic Inputs to the Serotonin and Dopamine Neuromodulatory Systems. Cell Rep. *8*, 1105–1118. https://doi.org/10.1016/j.celrep.2014.06.042.

Okaty, B.W., Commons, K.G., and Dymecki, S.M. (2019). Embracing diversity in the 5-HT neuronal system. Nat. Rev. Neurosci. *20*, 397–424. https://doi.org/10.1038/s41583-019-0151-3.

Okaty, B.W., Sturrock, N., Escobedo Lozoya, Y., Chang, Y., Senft, R.A., Lyon, K.A., Alekseyenko, O.V., and Dymecki, S.M. (2020). A single-cell transcriptomic and anatomic atlas of mouse dorsal raphe Pet1 neurons. ELife *9*, e55523. https://doi.org/10.7554/eLife.55523.

Pachernegg, S., Strutz-Seebohm, N., and Hollmann, M. (2012). GluN3 subunit-containing NMDA receptors: not just one-trick ponies. Trends Neurosci. *35*, 240–249. https://doi.org/10.1016/j.tins.2011.11.010.

Papageorgiou, G., and Corrie, J.E.T. (2000). Effects of Aromatic Substituents on the Photocleavage of 1-Acyl-7-nitroindolines. Tetrahedron *56*, 8197–8205. https://doi.org/10.1016/S0040-4020(00)00745-6.

Pollak Dorocic, I., Fürth, D., Xuan, Y., Johansson, Y., Pozzi, L., Silberberg, G., Carlén, M., and Meletis, K. (2014). A Whole-Brain Atlas of Inputs to Serotonergic Neurons of the Dorsal and Median Raphe Nuclei. Neuron *83*, 663–678. https://doi.org/10.1016/j.neuron.2014.07.002.

Rall, W. (1964). Theoretical Significance of Dendritic Trees for Neuronal Input-Output Relations. Neural Theory Model. Ed Reiss RF Stanf. Univ. Press Palo Alto https://doi.org/10.7551/mitpress/6743.003.0015.

Rall, W. (1967). Distinguishing theoretical synaptic potentials computed for different soma-dendritic distributions of synaptic input. J. Neurophysiol. *30*, 1138–1168.

Rall, W., and Rinzel, J. (1974). Transient Response in a Dendritic Neuron Model for Currrent Injected at One Branch. Biophys. J. *14*, 759–790.

Ren, J., Friedmann, D., Xiong, J., Liu, C.D., Ferguson, B.R., Weerakkody, T., DeLoach, K.E., Ran, C., Pun, A., Sun, Y., et al. (2018). Anatomically Defined and Functionally Distinct Dorsal Raphe Serotonin Sub-systems. Cell https://doi.org/10.1016/j.cell.2018.07.043.

Ren, J., Isakova, A., Friedmann, D., Zeng, J., Grutzner, S.M., Pun, A., Zhao, G.Q., Kolluru, S.S., Wang, R., Lin, R., et al. (2019). Single-cell transcriptomes and whole-brain projections of serotonin neurons in the mouse dorsal and median raphe nuclei. ELife *8*. https://doi.org/10.7554/eLife.49424.

Sancho, L., and Bloodgood, B.L. (2018). Functional Distinctions between Spine and Dendritic Synapses Made onto Parvalbumin-Positive Interneurons in Mouse Cortex. Cell Rep. *24*, 2075–2087. https://doi.org/10.1016/j.celrep.2018.07.070.

Smith, M.A., Ellis-Davies, G.C.R., and Magee, J.C. (2003). Mechanism of the distance-dependent scaling of Schaffer collateral synapses in rat CA1 pyramidal neurons. The Journal of Physiology 548, 245–258. 10.1113/jphysiol.2002.036376.

Soares, C., Lee, K.F.H., Nassrallah, W., and Beique, J.-C. (2013). Differential Subcellular Targeting of Glutamate Receptor Subtypes during Homeostatic Synaptic Plasticity. J. Neurosci. *33*, 13547–13559. https://doi.org/10.1523/JNEUROSCI.1873-13.2013.

Soares, C., Lee, K.F.H., and Béïque, J.-C. (2017). Metaplasticity at CA1 Synapses by Homeostatic Control of Presynaptic Release Dynamics. Cell Rep. *21*, 1293–1303. https://doi.org/10.1016/j.celrep.2017.10.025.

Soiza-Reilly, M., and Commons, K.G. (2011a). Glutamatergic drive of the dorsal raphe nucleus. J. Chem. Neuroanat. *41*, 247–255. https://doi.org/10.1016/j.jchemneu.2011.04.004.

Soiza-Reilly, M., and Commons, K.G. (2011b). Quantitative analysis of glutamatergic innervation of the mouse dorsal raphe nucleus using array tomography. J. Comp. Neurol. *519*, 3802–3814. https://doi.org/10.1002/cne.22734.

Song, J.H., Lucaci, D., Calangiu, I., Brown, M.T.C., Park, J.S., Kim, J., Brickley, S.G., and Chadderton, P. (2018). Combining mGRASP and Optogenetics Enables High-Resolution Functional Mapping of Descending Cortical Projections. Cell Rep. *24*, 1071–1080. https://doi.org/10.1016/j.celrep.2018.06.076.

Spruston, N., Jaffe, D.B., and Johnston, D. (1994). Dendritic attenuation of synaptic potentials and currents: the role of passive membrane properties. Trends Neurosci. *17*, 161–166. https://doi.org/10.1016/0166-2236(94)90094-9.

Stuart, G.J., and Häusser, M. (2001). Dendritic coincidence detection of EPSPs and action potentials. Nat. Neurosci. *4*, 63–71. https://doi.org/10.1038/82910.

Stuart, G.J., and Spruston, N. (2015). Dendritic integration: 60 years of progress. Nat. Neurosci. *18*, 1713–1721. https://doi.org/10.1038/nn.4157.

Takahashi, N., Oertner, T.G., Hegemann, P., and Larkum, M.E. (2016). Active cortical dendrites modulate perception. Science *354*, 1587–1590. https://doi.org/10.1126/science.aah6066.

Tran-Van-Minh, A., Cazé, R.D., Abrahamsson, T., Cathala, L., Gutkin, B.S., and DiGregorio, D.A. (2015). Contribution of sublinear and supralinear dendritic integration to neuronal computations. Front. Cell. Neurosci. *9*. https://doi.org/10.3389/fncel.2015.00067.

Tran-Van-Minh, A., Abrahamsson, T., Cathala, L., and DiGregorio, D.A. (2016). Differential Dendritic Integration of Synaptic Potentials and Calcium in Cerebellar Interneurons. Neuron *91*, 837–850. https://doi.org/10.1016/j.neuron.2016.07.029.

Traynelis, S.F., Wollmuth, L.P., McBain, C.J., Menniti, F.S., Vance, K.M., Ogden, K.K., Hansen, K.B., Yuan, H., Myers, S.J., and Dingledine, R. (2010). Glutamate Receptor Ion Channels: Structure, Regulation, and Function. Pharmacol. Rev. *62*, 405–496. https://doi.org/10.1124/pr.109.002451.

van der Walt, S., Colbert, S.C., and Varoquaux, G. (2011). The NumPy Array: A Structure for Efficient Numerical Computation. Comput. Sci. Eng. *13*, 22–30. https://doi.org/10.1109/MCSE.2011.37.

Warden, M.R., Selimbeyoglu, A., Mirzabekov, J.J., Lo, M., Thompson, K.R., Kim, S.-Y., Adhikari, A., Tye, K.M., Frank, L.M., and Deisseroth, K. (2012). A prefrontal cortex–brainstem neuronal projection that controls response to behavioural challenge. Nature *492*, 428–432. https://doi.org/10.1038/nature11617.

Weissbourd, B., Ren, J., DeLoach, K.E., Guenthner, C.J., Miyamichi, K., and Luo, L. (2014). Presynaptic Partners of Dorsal Raphe Serotonergic and GABAergic Neurons. Neuron *83*, 645–662. https://doi.org/10.1016/j.neuron.2014.06.024.

Yuste, R. (2011). Dendritic Spines and Distributed Circuits. Neuron *71*, 772–781. https://doi.org/10.1016/j.neuron.2011.07.024.

Zhong, W., Li, Y., Feng, Q., and Luo, M. (2017). Learning and Stress Shape the Reward Response Patterns of Serotonin Neurons. J. Neurosci. *37*, 8863–8875. https://doi.org/10.1523/JNEUROSCI.1181-17.2017.

Zhou, L., Liu, M.-Z., Li, Q., Deng, J., Mu, D., and Sun, Y.-G. (2017). Organization of Functional Long-Range Circuits Controlling the Activity of Serotonergic Neurons in the Dorsal Raphe Nucleus. Cell Rep. *18*, 3018–3032. https://doi.org/10.1016/j.celrep.2017.02.077.

A. Supplementary Figure

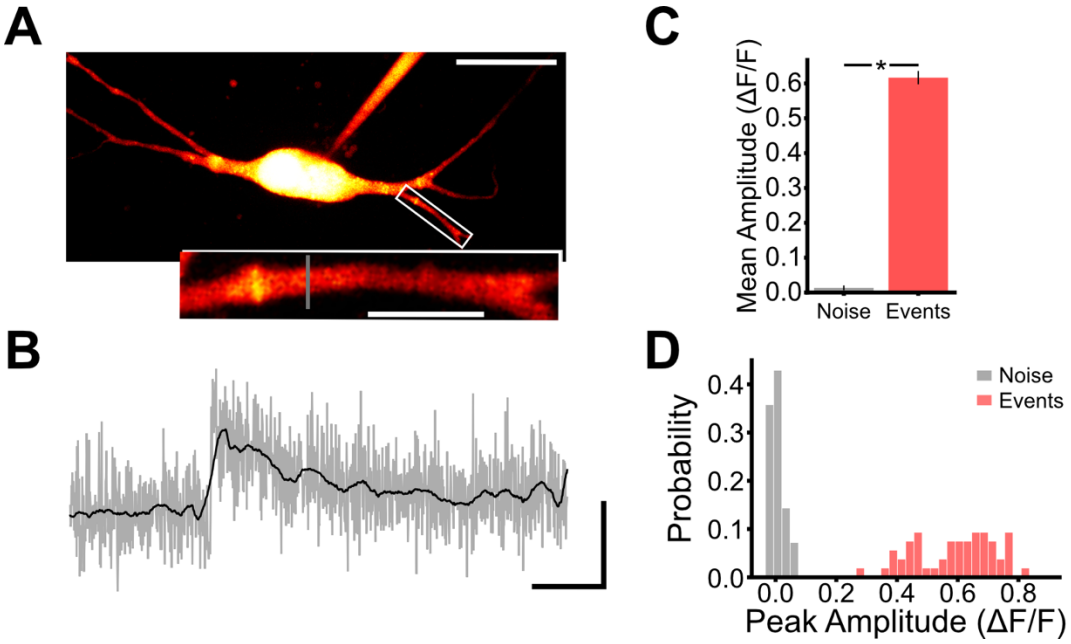

Figure S1. Backpropagating Action Potential in 5-HT Neurons.
(A) High-magnification multi-photon image of a dendritic segment of a DRN 5-HT neuron with morphological marker Alexa 594 (scale bar; 30 microns). High-magnification image of the dendritic segment (below) marked by the white box (scale bar; 10 microns). Grey line shows the location of the line scan. (B) Resulting calcium signals elicited from backpropagating action potential (bAP) (grey signal). Average calcium signal (black line) (scale bar; 0.4 Δ F/F / 200 ms). (C) Mean amplitude ± SEM of recorded calcium signals (red bar) and baseline noise (grey bar). (B) Plotted distributions of the baseline noise for each dendrites and all the calcium events. Star indicate $p < 0.05$. 56 events from 14 dendrites and 6 neurons.